2017

Differential Cross Section Measurements for γn→π-p Above the First Nucleon Resonance Region

P. T. Mattione

D. S. Carman

I. I. Strakovsky

R. L. Workman

A. E. Kudryavtsev

See next page for additional authors

Authors

P. T. Mattione, D. S. Carman, I. I. Strakovsky, R. L. Workman, A. E. Kudryavtsev, A. Svarc, V. E. Tarasov, K. P. Adhikari, S. Adhikari, D. Adikaram, G. Charles, M. Khachatryan, A. Klein, Y. Prok, and Z. W. Zhao

Differential cross section measurements for $\gamma n \to \pi^- p$ above the first nucleon resonance region

P. T. Mattione,[1] D. S. Carman,[1] I. I. Strakovsky,[20] R. L. Workman,[20] A. E. Kudryavtsev,[30] A. Svarc,[29] V. E. Tarasov,[30]
K. P. Adhikari,[33] S. Adhikari,[16] D. Adikaram,[1,37] Z. Akbar,[17] S. Anefalos Pereira,[24] J. Ball,[8] N. A. Baltzell,[1,41]
M. Bashkanov,[13] M. Battaglieri,[25] V. Batourine,[1,32] I. Bedlinskiy,[30] A. S. Biselli,[15] S. Boiarinov,[1] W. J. Briscoe,[20]
V. D. Burkert,[1] T. Cao,[21,41] A. Celentano,[25] G. Charles,[37] T. Chetry,[36] G. Ciullo,[14,23] L. Clark,[19] P. L. Cole,[22] M. Contalbrigo,[23]
O. Cortes,[22] V. Crede,[17] A. D'Angelo,[26,39] N. Dashyan,[47] R. De Vita,[25] E. De Sanctis,[24] M. Defurne,[8] A. Deur,[1] C. Djalali,[41]
M. Dugger,[3] R. Dupre,[28] H. Egiyan,[1] A. El Alaoui,[43] L. El Fassi,[33] P. Eugenio,[17] G. Fedotov,[40,41] R. Fersch,[9] A. Filippi,[27]
J. A. Fleming,[13] A. Fradi,[11,28] Y. Ghandilyan,[47] G. P. Gilfoyle,[38] K. L. Giovanetti,[31] F. X. Girod,[1] C. Gleason,[41] E. Golovatch,[40]
R. W. Gothe,[41] K. A. Griffioen,[46] M. Guidal,[28] K. Hafidi,[2] H. Hakobyan,[43,47] C. Hanretty,[1] N. Harrison,[1] M. Hattawy,[2]
D. Heddle,[9,1] K. Hicks,[36] G. Hollis,[41] M. Holtrop,[34] S. M. Hughes,[13] Y. Ilieva,[20,41] D. G. Ireland,[19] B. S. Ishkhanov,[40]
E. L. Isupov,[40] D. Jenkins,[44] H. Jiang,[41] H. S. Jo,[28] K. Joo,[10] S. Joosten,[42] D. Keller,[45] G. Khachatryan,[47] M. Khachatryan,[37]
M. Khandaker,[22,35] A. Kim,[10] W. Kim,[32] A. Klein,[37] F. J. Klein,[7] V. Kubarovsky,[1] S. V. Kuleshov,[30,43] L. Lanza,[26] P. Lenisa,[23]
K. Livingston,[19] I. J. D. MacGregor,[19] N. Markov,[10] B. McKinnon,[19] C. A. Meyer,[6] Z. E. Meziani,[42] T. Mineeva,[43]
V. Mokeev,[1,40] R. A. Montgomery,[19] A. Movsisyan,[23] C. Munoz Camacho,[28] G. Murdoch,[19] P. Nadel-Turonski,[1,20] L. A. Net,[41]
S. Niccolai,[28] G. Niculescu,[31] I. Niculescu,[31] M. Osipenko,[25] A. I. Ostrovidov,[17] M. Paolone,[42] R. Paremuzyan,[34] K. Park,[1]
E. Pasyuk,[1] W. Phelps,[16] S. Pisano,[24] O. Pogorelko,[30] J. W. Price,[4] S. Procureur,[8] Y. Prok,[37,45] D. Protopopescu,[19]
B. A. Raue,[1,16] M. Ripani,[18] B. G. Ritchie,[3] A. Rizzo,[26,39] G. Rosner,[19] F. Sabatié,[8] C. Salgado,[35] R. A. Schumacher,[6]
Y. G. Sharabian,[1] A. Simonyan,[47] Iu. Skorodumina,[40,41] G. D. Smith,[13] D. Sokhan,[19] N. Sparveris,[42] I. Stankovic,[13]
S. Stepanyan,[1] S. Strauch,[41] M. Taiuti,[18,25] M. Ungaro,[1,10] H. Voskanyan,[47] E. Voutier,[28] N. K. Walford,[7] D. Watts,[13] X. Wei,[1]
M. H. Wood,[5,41] N. Zachariou,[13] J. Zhang,[1] and Z. W. Zhao[12,37]

(CLAS Collaboration)

[1]*Thomas Jefferson National Accelerator Facility, Newport News, Virginia 23606, USA*
[2]*Argonne National Laboratory, Argonne, Illinois 60439, USA*
[3]*Arizona State University, Tempe, Arizona 85287, USA*
[4]*California State University, Dominguez Hills, Carson, California 90747, USA*
[5]*Canisius College, Buffalo, New York 14208, USA*
[6]*Carnegie Mellon University, Pittsburgh, Pennsylvania 15213, USA*
[7]*The Catholic University of America, Washington, DC 20064, USA*
[8]*CEA, Centre de Saclay, Irfu/Service de Physique Nucléaire, 91191 Gif-sur-Yvette, France*
[9]*Christopher Newport University, Newport News, Virginia 23606, USA*
[10]*University of Connecticut, Storrs, Connecticut 06269, USA*
[11]*University of Dammam, Industrial Jubail 31961, Saudi Arabia*
[12]*Duke University, Durham, North Carolina 27708-0305, USA*
[13]*Edinburgh University, Edinburgh EH9 3JZ, United Kingdom*
[14]*Universita' di Ferrara, 44121 Ferrara, Italy*
[15]*Fairfield University, Fairfield, Connecticut 06824, USA*
[16]*Florida International University, Miami, Florida 33199, USA*
[17]*Florida State University, Tallahassee, Florida 32306, USA*
[18]*Università di Genova, 16146 Genova, Italy*
[19]*University of Glasgow, Glasgow G12 8QQ, United Kingdom*
[20]*The George Washington University, Washington, DC 20052, USA*
[21]*Hampton University, Hampton, Virginia 23668, USA*
[22]*Idaho State University, Pocatello, Idaho 83209, USA*
[23]*INFN, Sezione di Ferrara, 44100 Ferrara, Italy*
[24]*INFN, Laboratori Nazionali di Frascati, 00044 Frascati, Italy*
[25]*INFN, Sezione di Genova, 16146 Genova, Italy*
[26]*INFN, Sezione di Roma Tor Vergata, 00133 Rome, Italy*
[27]*INFN, Sezione di Torino, 10125 Torino, Italy*
[28]*Institut de Physique Nucléaire ORSAY, Orsay, France*
[29]*Rudjer Bošković Institute, Bijenička Cesta 10002 Zagreb, Croatia*
[30]*National Research Center Kurchatov Institute, Institute of Theoretical and Experimental Physics, Moscow 117218, Russia*
[31]*James Madison University, Harrisonburg, Virginia 22807, USA*
[32]*Kyungpook National University, Daegu 702-701, Republic of Korea*
[33]*Mississippi State University, Mississippi State, Mississippi 39762-5167, USA*
[34]*University of New Hampshire, Durham, New Hampshire 03824, USA*
[35]*Norfolk State University, Norfolk, Virginia 23504, USA*
[36]*Ohio University, Athens, Ohio 45701, USA*

[37]*Old Dominion University, Norfolk, Virginia 23529, USA*
[38]*University of Richmond, Richmond, Virginia 23173, USA*
[39]*Universita' di Roma Tor Vergata, 00133 Rome, Italy*
[40]*Skobeltsyn Nuclear Physics Institute, 119899 Moscow, Russia*
[41]*University of South Carolina, Columbia, South Carolina 29208, USA*
[42]*Temple University, Philadelphia, Pennsylvania 19122, USA*
[43]*Universidad Técnica Federico Santa María, Casilla 110-V Valparaíso, Chile*
[44]*Virginia Tech, Blacksburg, Virginia 24061-0435, USA*
[45]*University of Virginia, Charlottesville, Virginia 22901, USA*
[46]*College of William and Mary, Williamsburg, Virginia 23187, USA*
[47]*Yerevan Physics Institute, 375036 Yerevan, Armenia*

The quasifree $\gamma d \to \pi^- p(p)$ differential cross section has been measured with CLAS at photon beam energies E_γ from 0.445 to 2.510 GeV (corresponding to W from 1.311 to 2.366 GeV) for pion center-of-mass angles $\cos\theta_\pi^{c.m.}$ from -0.72 to 0.92. A correction for final state interactions has been applied to these data to extract the $\gamma n \to \pi^- p$ differential cross sections. These cross sections are quoted in 8428 (E_γ, $\cos\theta_\pi^{c.m.}$) bins, a factor of nearly 3 increase in the world statistics for this channel in this kinematic range. These new data help to constrain coupled-channel analysis fits used to disentangle the spectrum of N^* resonances and extract their properties. Selected photon decay amplitudes $N^* \to \gamma n$ at the resonance poles are determined for the first time and are reported here.

I. INTRODUCTION

The determination of the resonance properties for all accessible baryon states is a central objective in nuclear physics. The extracted resonance parameters provide a crucial body of information for understanding the nucleon excitation spectrum and for testing models of the nucleon inspired by quantum chromodynamics (QCD) and, more recently, lattice QCD calculations. The spectrum of N^* and Δ^* baryon resonances has been extensively studied through meson-nucleon scattering and meson photoproduction experiments. Properties of the known resonances continue to become better determined as experiments involving polarized beams, targets, and recoil measurements are expanded and refined [1]. Extracted quantities include resonance masses, widths, branching fractions, pole positions, and associated residues, as well as photodecay amplitudes [2]. New states have also been found, mainly through multichannel analyses that are sensitive to states having a relatively weak coupling to the πN decay channel [3–5].

Knowledge of the N^* and Δ^* resonance photodecay amplitudes has largely been restricted to the charged states. Apart from lower-energy inverse reaction $\pi^- p \to \gamma n$ measurements, the extraction of the two-body $\gamma n \to \pi^- p$ and $\gamma n \to \pi^0 n$ observables requires the use of a model-dependent nuclear correction, which mainly comes from final state interaction (FSI) effects within the target deuteron. Most γn data are unpolarized and cover fairly narrow energy ranges. Of these, only about 400 $\pi^0 n$ measurement data points exist, spanning the full nucleon resonance region [6].

The importance of improving the γn database relative to the γp database is directly related to the fact that the electromagnetic interaction does not conserve isospin symmetry. The amplitude for the reactions $\gamma N \to \pi X$ factors into distinct $I = 1/2$ and $I = 3/2$ isospin components, $A_{\gamma,\pi^\pm} = \sqrt{2}(A_{p/n}^{I=1/2} \mp A^{I=3/2})$. This expression indicates that the ex-

citation of the $I = 3/2$ Δ^* states can be entirely determined from proton target data. However, measurements from datasets with both neutron and proton targets are required to determine the isospin $I = 1/2$ amplitudes and to separate the $\gamma p N^*$ and $\gamma n N^*$ photocouplings.

This work focuses on negative pion photoproduction off the neutron using a deuteron target. A large body of new precision $\gamma n \to \pi^- p$ differential cross sections for $E_\gamma = 0.445$ to 2.510 GeV in laboratory photon energy, corresponding to an invariant energy range from $W = 1.311$ to 2.366 GeV, are reported. Pion center-of-mass (c.m.) production angles, ranging from $\theta_\pi^{c.m.} = 26°$ to $135°$, have been measured during the CLAS Collaboration g13 run period [7]. These new cross section data have nearly tripled the world $\gamma n \to \pi^- p$ database below $E_\gamma = 2.700$ GeV [6].

The $\gamma n \to \pi^- p$ differential cross section was previously measured by the CLAS g10 [8] experiment. Those measurements contained 855 data points in 50- and 100-MeV-wide bins of beam energy E_γ from 1.050 to 3.500 GeV, corresponding to a W range from 1.690 to 2.731 GeV. However, the 8428 data points from g13 are a precision measurement of this cross section, with a factor of $\sim$10 increase in data points. These data are reported in 10- and 20-MeV-wide bins of beam energy E_γ, with overall normalization uncertainties of $\sim$3.4%, compared to the $\sim$6% to $\sim$10% overall normalization uncertainties achieved by g10. Also, unlike the g10 measurements, the g13 data cover the W range of the low-mass N^* resonances, and can be used to investigate their helicity amplitudes and resonance parameters.

The present dataset, together with completed polarized measurements for both $\pi^- p$ and $\pi^0 n$ from Jefferson Lab [9] and MAMI [10], are expected to lead to the determination of well-constrained γn decay amplitudes in the near future. However, these new CLAS $\gamma n \to \pi^- p$ data allow for the first determination of selected photon decay amplitudes $N^* \to \gamma n$ at their pole on the complex plane.

The organization for this paper is as follows. In Sec. II, details of the g13 experiment and the CLAS detector are provided. Section III outlines the event selection and Sec. IV provides the tracking and triggering efficiency corrections. Section V describes the extraction of the event yields and the acceptance corrections, and Sec. VI describes how the beam-target luminosity was determined. Section VII presents and discusses the measured differential cross sections for the reaction $\gamma n \to \pi^- p$, while Sec. VIII reviews the approach for determining the final state interaction corrections. Sections IX and X describe the Legendre fits and multipole fit results, respectively. Finally, Sec. XI provides a summary of this work and the conclusions.

II. EXPERIMENT

The CLAS g13 experiment [7] ran from October 2006 to June 2007 in Hall B at the Continuous Electron Beam Accelerator Facility (CEBAF) at Jefferson Lab in Newport News, Virginia. Circularly and linearly polarized tagged bremsstrahlung photon beams were incident on a liquid-deuterium (LD$_2$) target located near the center of the CLAS detector [11]. The circularly polarized photon beam portion of this experiment, called g13a, was used for this analysis.

For g13a, the CEBAF electron beam was supplied at two different energies, 1.990 and 2.655 GeV. These electrons were delivered at currents between 33 and 45 nA in beam bunches separated by about 2 ns. The electron beam was incident on a 10^{-4} radiation-length-thick gold foil radiator to produce the bremsstrahlung photon beam.

The dipole magnet of the Hall B photon tagger deflected the electron beam and postbremsstrahlung electrons in order to tag photons produced with energies between $\sim 20\%$ and $\sim 95\%$ of the incident electron beam energy [12]. The tagging system provided a photon beam energy resolution of $\sim 0.1\%$ of the electron beam energy with a 150-ps timing resolution. A 6.4-mm-diameter nickel collimator downstream of the radiator provided $\sim 90\%$ beam transmission to the 40-cm-long LD$_2$ target, which was centered 20 cm upstream from the center of the CLAS detector. This resulted in a tagged photon flux on the order of 10^7 Hz on the target.

The CLAS detector, shown in Fig. 1, was designed around six superconducting coils arranged in a hexagonal configuration that produced an approximately toroidal magnetic field surrounding the beamline. The magnetic field bent charged particles through the three regions of multilayer drift chambers for momentum measurements. The drift chambers were positioned between the superconducting coils within six sectors in azimuthal ϕ, each spanning roughly $60°$. Charged particles produced at a momentum of 1 GeV/c were measured with a momentum resolution of $\sigma(p)/p \leqslant 0.5\%$, and with average angular resolutions in the fiducial volume of $\sigma(\theta)$, $\sigma(\phi) \sim 2$ mrad [13]. For the g13 experiment, the torus magnet operated at $\sim 40\%$ of its maximum current with reversed field polarity (such that negatively charged particles were bent away from the beamline), producing an integrated magnetic field of 0.972 T m along the track path length at forward angles and 0.233 T m at $90°$.
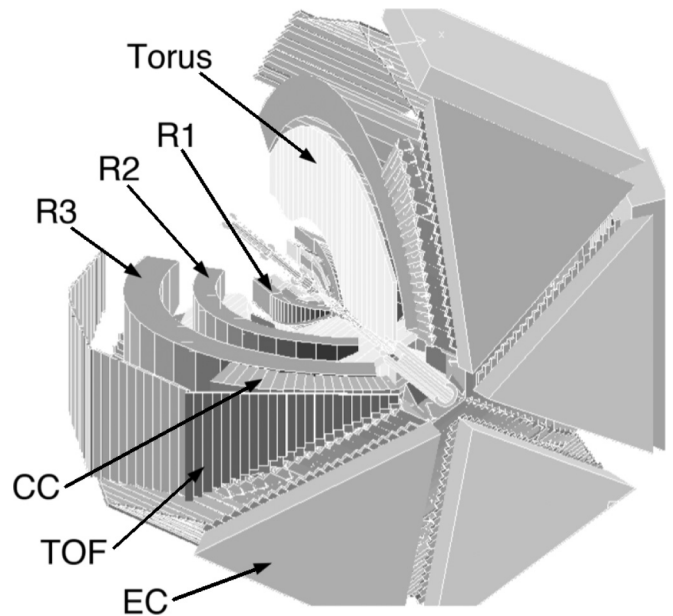

FIG. 1. Cutaway view of the CLAS detector [11] illustrating the torus magnet, three regions of drift chambers (R1–R3), Cherenkov counters (CC), time-of-flight scintillators (TOF), and electromagnetic calorimeters (EC). The CLAS detector is roughly 10 m in diameter.

The start counter (ST) surrounding the target had a timing resolution of 260 ps, and was used to determine which of the 2-ns electron beam bunches was associated with the recorded physics event [14]. The time-of-flight (TOF) scintillator paddles had a timing resolution between 150 and 250 ps, depending on the length of the paddle, and were used for particle identification [15]. At forward angles, Cherenkov counters (not used for this experiment) could be used to identify electrons [16], and the electromagnetic calorimeters could be used to detect electrons and neutral particles [17].

A coincidence between the start counter and TOF scintillators in at least two of the six CLAS sectors was required for triggering of the data acquisition. With slightly more than two months of running, 20 billion physics events were recorded in the g13a dataset.

III. EVENT SELECTION

The $\gamma d \to \pi^- p(p)$ differential cross section was measured separately for the 1.990- and 2.655-GeV beam data, and these cross section results were combined as discussed in Sec. VII. The yields of the $\gamma d \to \pi^- p(p)$ reaction were determined by reconstructing the π^- and scattered (higher momentum) proton, with the lower momentum proton missing. The proton in the deuteron typically has a momentum from Fermi motion of less than 200 MeV/c [18] (and peaks at ~ 50 MeV/c), and was often stopped before it could escape the LD$_2$ target.

The reconstructed beam energy and track momenta were slightly distorted by effects not taken into account during the event reconstruction. These effects included uncertainties in the incident electron beam energy, unaccounted for energy losses as the tracks traversed the detector, and drift chamber misalignments and inaccuracies in the magnetic field map that
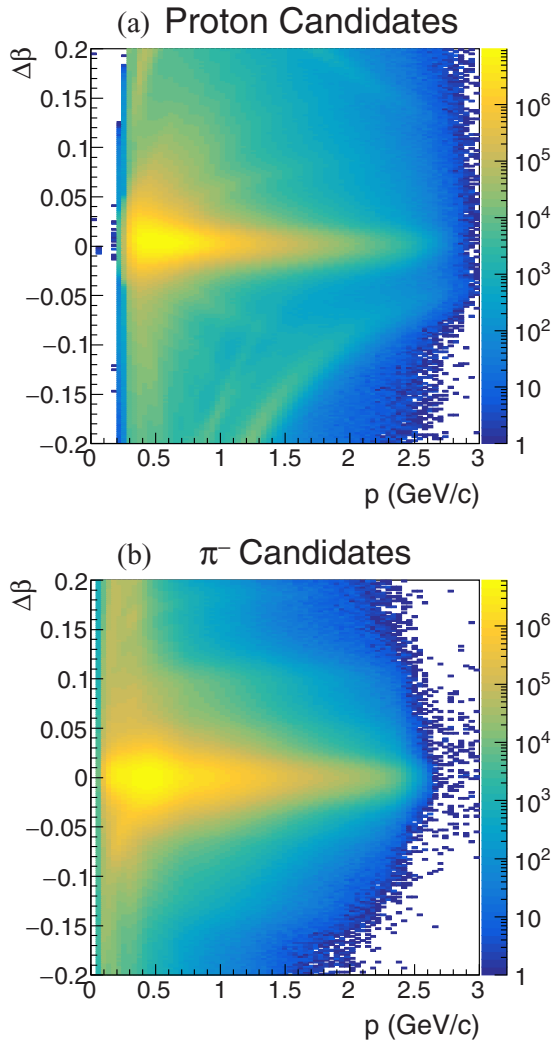
(a) Proton Candidates

(b) π^- Candidates

FIG. 2. $\Delta\beta$ vs momentum for proton (a) and π^- (b) candidates. $\Delta\beta$ is centered at zero for the protons and π^-'s, and the neighboring bands are from other particle types, such as π^+'s, or from choosing the wrong beam bunch.

affected the reconstructed track momenta. Each of these effects was studied and resulted in beam energy and track momentum corrections on the order of a few percent [19].

A. Particle identification

Initially, all reconstructed positively and negatively charged tracks were treated as candidates for the proton and π^-, respectively. Then, for each combination of proton and π^- candidates, their start counter hits were used to select the beam bunch corresponding to the event. The arrival time of the beam bunches was known to a resolution of 50 ps, and was used as a reference time for the particle identification. Figure 2 shows the $\Delta\beta$ vs momentum distributions of the proton and π^- candidates, where $\Delta\beta$ is the difference between $\beta = p/E$ using the candidate mass, and β determined from the track path length (from the event vertex to the TOF system) and the track hit time from the TOF paddle. $\Delta\beta$ is centered at zero for the protons and π^-'s, and the neighboring bands are from
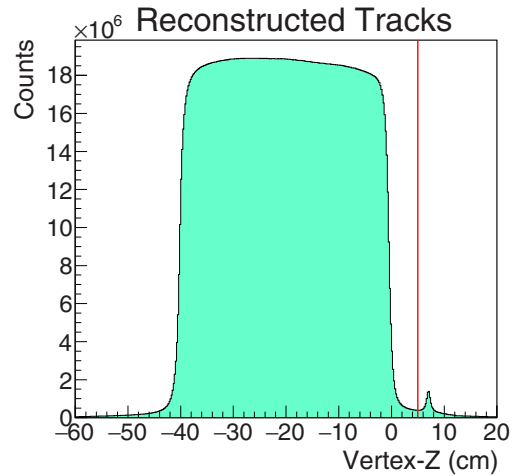
Reconstructed Tracks

FIG. 3. The vertex z of the reconstructed tracks in $\gamma d \to \pi^- p(p)$. Tracks with $z > 5$ cm were cut, removing backgrounds from the aluminum end cap of the target assembly at $z = 7$ cm.

other particle types, such as π^+'s, or from choosing the wrong beam bunch.

For proton identification, a momentum-dependent $\pm 5\sigma$ cut was applied on $\Delta\beta$. No particle identification cut was used to identify π^-'s since the background from electron, muon, and kaon events was negligible, as seen in Fig. 2(b). Poorly performing or miscalibrated TOF counters were excluded from the analysis.

B. Vertex cuts and missing momentum

The vertex-z distribution of the reconstructed tracks, defined as their distance-of-closest-approach to the nominal beamline (defined as the z axis), is shown in Fig. 3. A cut was applied requiring that the reconstructed vertex z of both the proton and the π^- be less than 5 cm. The target extended from -40 to 0 cm in vertex z, so this cut was used to remove backgrounds from beam photons striking the aluminum end cap of the target assembly.

To illustrate the missing momentum distribution of $\gamma d \to \pi^- p(p)$ events, a $\pm 3\sigma$ cut was applied around the missing mass peak of the proton. Figure 4(a) shows the missing momentum distribution after this cut. The missing momentum is primarily peaked at low momenta due to Fermi motion, and the high-momentum tail is primarily from rescattering events. Figure 4(b) shows that the slow-proton momentum is uniformly distributed in $\cos\theta$, where θ is the angle between the missing momentum and the beam in the laboratory frame. A cut was applied at 200 MeV/c to reject the majority of the rescattering events. Since there are still rescattering effects present after this cut, the $\gamma d \to \pi^- p(p)$ cross section is quoted as "quasifree."

IV. CLAS EFFICIENCY STUDIES

A. Tracking efficiency

To determine the charged particle tracking efficiency, the CLAS drift chamber wire hit efficiencies were studied by
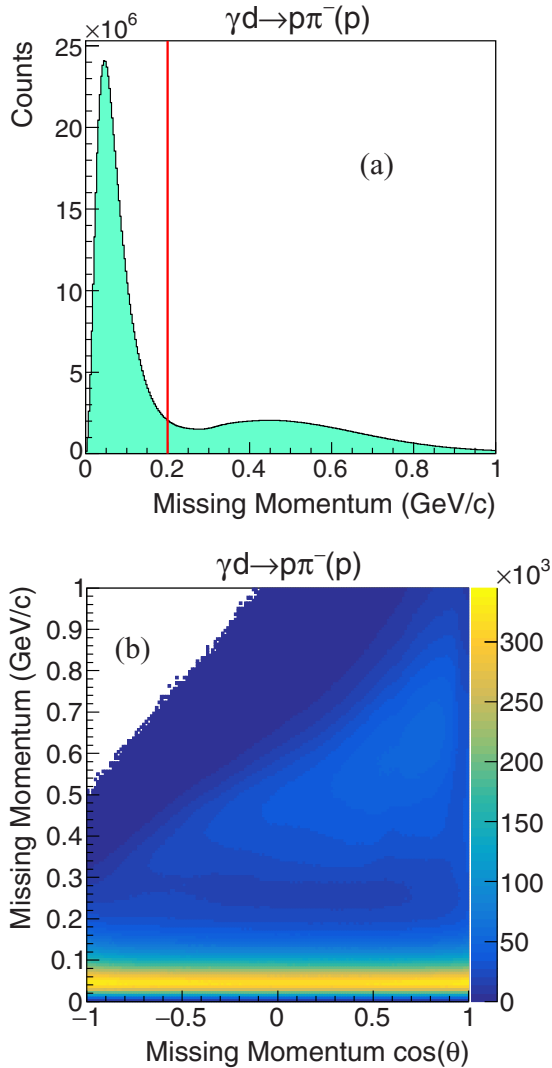
FIG. 4. (a) The $\gamma d \to \pi^- p(p)$ missing momentum and (b) the same missing momentum vs $\cos\theta$ of the missing momentum in the laboratory frame. The low-momentum, quasifree protons followed the Fermi motion distribution and were relatively uniformly distributed in $\cos\theta$. The high-momentum tail of rescattered protons was removed by the 200-MeV/c cut on the missing momentum [indicated by the red vertical line in (a)].

determining how often a given sense wire recorded a hit when a reconstructed track passed nearby. To make sure that the study was unbiased, the efficiencies were only evaluated when there were significantly more hits on the track than the minimum needed for reconstruction.

These studies allowed issues associated with missing wires due to bad high-voltage connections and amplifier low-voltage shorts to be taken into account. Furthermore, these studies were able to determine tracking inefficiencies due to readout electronics problems, cable disconnects, and cable swaps. Groups of wires that were correlated with a common problem were grouped together in the simulation so that they were either kept or rejected as a whole. The efficiency calculated and applied for the regions with cable swaps or disconnects

does not properly model the experimental data, so these regions were eliminated from the analysis. In this manner a very good match of the tracking efficiency in the simulation code to the CLAS hardware was possible. A comparison of the tracking efficiencies for each CLAS drift chamber sector is available in Ref. [19].

The track reconstruction efficiencies for protons and π^-'s were studied by analyzing the $\gamma d \to \pi^- p(p)$ and $\gamma d \to pp(\pi^-)$ topologies, respectively, and determining how often the missing particle was reconstructed when it was in the fiducial region of the detector. These studies were performed with both experimental and phase-space Monte Carlo (MC) simulated data as a function of track momentum and direction. For the g13 experiment, these reconstruction efficiencies were 95% or higher in the nominal fiducial regions of the detector. Figure 5 shows the ratio of these reconstruction efficiencies ε for the proton, which was computed as

$$\varepsilon_{\text{Ratio}} = \frac{\varepsilon_{\text{Simulation}} - \varepsilon_{\text{Experiment}}}{\varepsilon_{\text{Experiment}}}. \tag{1}$$

Thus, regions with an efficiency ratio significantly greater (less) than zero are regions where the reconstruction efficiency was much lower (higher) in the experiment than in the MC simulation. The discrepancies seen in the figure at the edges of the acceptance are due to a mismatch between the simulated and experimental geometry. These regions were cut from the analysis so that only regions that were accurately modeled in the simulation were included in the cross section measurement. The efficiency ratio distributions for the π^-'s, which were bent differently in the CLAS magnetic field, are similar but required separate cuts. The absolute minimum accepted proton and π^- momenta were 360 and 100 MeV/c, respectively.

B. Triggering efficiency

As discussed in Sec. II, the g13a trigger was designed to record events with a ST and TOF coincidence in at least two sectors of CLAS. To determine the triggering efficiency, the $\gamma d \to \pi^- pp$ topology was studied, with the requirement that the three final state particles be in different sectors. For every pair of particles that registered as contributing to the trigger, the triggering rate of the third particle was studied.

Figure 6 shows the proton and π^- triggering efficiencies in a representative sector, as a function of the track angle and momentum. Because these efficiencies were studied as a function of all kinematics, they include both TOF and ST efficiency effects. The proton triggering was efficient in general, but was low in a few of the TOF paddles, due to one or both of the photomultiplier tubes (PMTs) at the end of the scintillators having low gain.

However, the π^- efficiencies were significantly worse than those of the proton. This was because π^-'s deposited much less energy than protons of the same momentum in the scintillators, due to their higher velocity. A number of inefficient channels were present due to low gain TOF PMTs (even though they were set at their maximum voltage). These PMTs were still efficient for hit readout, as the 100-mV triggering threshold was much higher than the 20-mV detection threshold. The efficiencies for the other sectors are available in Ref. [19]. These
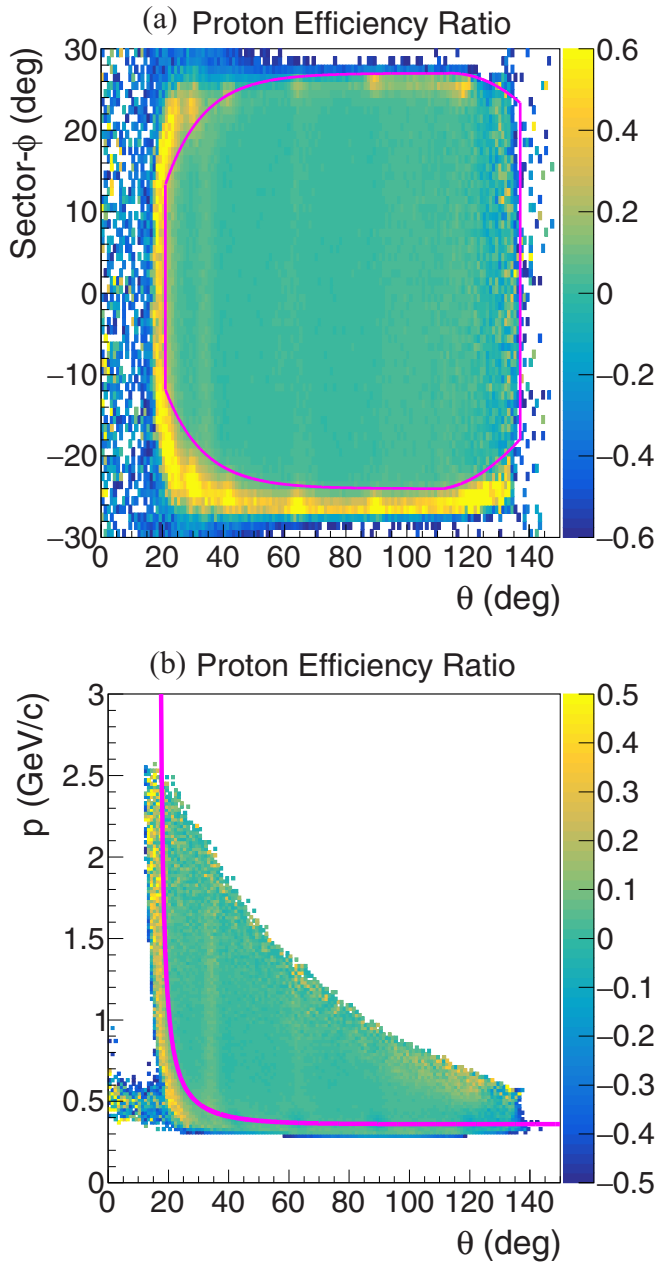
(a) Proton Efficiency Ratio

(b) Proton Efficiency Ratio

FIG. 5. The proton reconstruction efficiency ratio defined by Eq. (1) as a function of laboratory polar angle. In (a), sector ϕ is the azimuthal angle relative to the center of the CLAS sector. Both plots are summed over all CLAS sectors. The magenta lines indicate the cuts used to reject data that were not accurately modeled by the simulation.

FIG. 6. The proton (a) and π^- (b) triggering efficiencies in CLAS sector 2 in terms of momentum p vs laboratory polar angle θ. The proton triggering was efficient in general, but the π^- efficiency was affected over portions of the acceptance due to low-gain TOF PMTs.

triggering efficiencies were applied to the MC simulation to model these event losses.

V. YIELDS AND ACCEPTANCE

The $\gamma d \to \pi^- p(p)$ data were separated into 10- and 20-MeV-wide E_γ bins and 0.02- to 0.04-wide bins in $\cos \theta_\pi^{c.m.}$, where $\theta_\pi^{c.m.}$ is the angle between the π^- and the beam in the $\pi^- p$ c.m. frame. These data spanned the range from 0.440 to
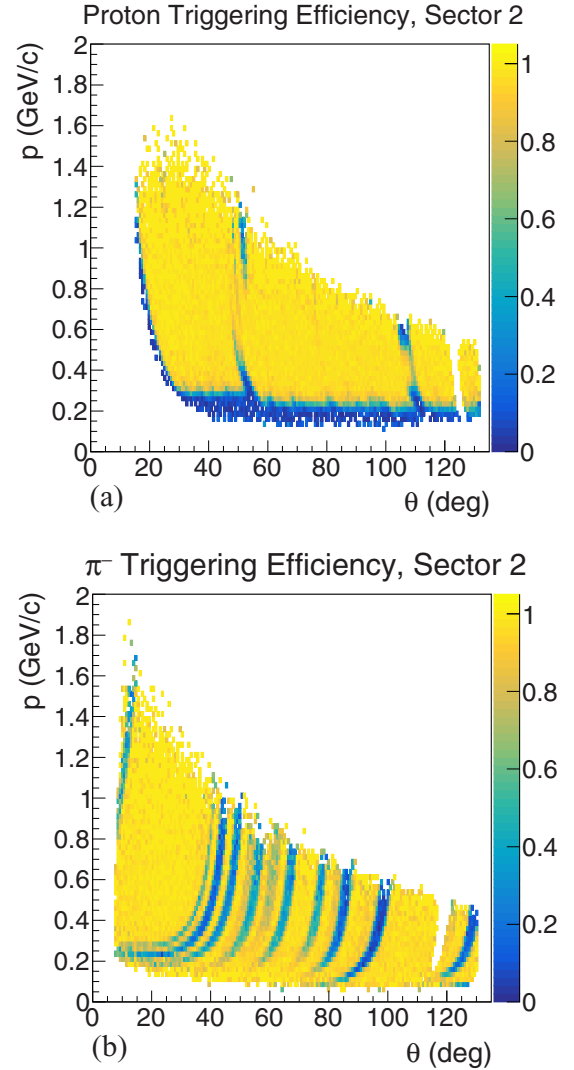
2.520 GeV in beam energy and -0.72 to 0.92 in $\cos \theta_\pi^{c.m.}$ for a total of 8428 bins. In each bin, the missing-proton peaks were fit to double-Gaussian functions over a linear background, an example of which is shown in Fig. 7. A double-Gaussian function is defined as the sum of two Gaussians with identical means, but different heights and widths. The larger, primary Gaussian was used to model the Gaussian-scattering portion of the signal distribution, and the smaller, secondary Gaussian was used to fit the tails of the signal distribution.

The backgrounds are primarily due to misidentified protons and π^-'s, or selection of the wrong beam photon. The $\gamma d \to \pi^- p(p)$ yield was defined as the number of events above the background within the $\pm 4.5\sigma$ fit range about the missing-proton peak. There were over 400 million $\gamma d \to \pi^- p(p)$ events in the g13a experimental data sample used for this analysis.
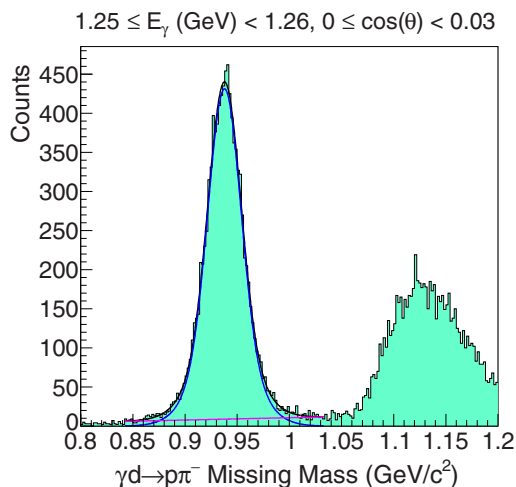
FIG. 7. Sample fit of the missing-proton peak in the missing mass off of $\gamma d \to \pi^- p$. The signals were fit to a double-Gaussian function over a linear background. The blue line shape represents the double-Gaussian fit function, the magenta line shape represents the linear fit function, and the black line shape represents the total fit function.

FIG. 8. A comparison of the reconstructed $\gamma d \to \pi^- p(p)$ yields between the experimental data (black) and the simulation (red) as a function of the pion c.m. angle $\cos \theta_\pi^{c.m.}$ in two selected beam energy bins for the 2.655-GeV data. The simulated yields have been scaled such that their integral matches that of the experimental data.

A total of 1.8 billion MC $\gamma d \to \pi^- pp$ events were simulated for each electron beam energy to calculate the acceptance corrections. These data were evaluated separately in order to individually compute the cross sections for the different run ranges. The George Washington University (GWU) SAID GB12 cross section predictions [8], based on the world data of the $\gamma n \to \pi^- p$ reaction, were used to generate the event distributions. After a preliminary quasifree $\gamma d \to \pi^- p(p)$ cross section measurement was obtained from the g13 data, this measurement was used to generate the final simulated data. A comparison of the reconstructed $\gamma d \to \pi^- p(p)$ yield between the experimental data and the MC is shown in Fig. 8. This shows that the inefficient regions of the detector are well modeled by the simulation. Thus, any variations of the detector acceptance across the widths of the narrow yield-extraction bins did not cause an incorrect modeling of the CLAS acceptance.

The same analysis procedure and cuts used to select the $\gamma d \to \pi^- p(p)$ final state in the experimental data were used for the simulated data. However, a $\sim 5\%$ yield correction factor Y_{CF} was applied to the experimental yields to correct for event losses from choosing the incorrect beam bunch, which was not modeled in the simulation. This correction factor was determined by studying the $\gamma d \to \pi^- p(p)$ yield from all other beam bunches recorded in the event. The uncertainties on this correction factor were $\sim 0.003\%$ from statistics and $\sim 0.88\%$ from systematics, determined by studying the variation in the correction factor with beam energy.

Since the CLAS acceptance rapidly falls off near the edges of the detector, cross section measurements in these regions had systematic uncertainties that were difficult to quantify. In addition, small mismatches between the generated MC distribution and the experimental data could cause large uncertainties in regions of low acceptance. To remove these regions, bins with an acceptance less than 20% of the maximum
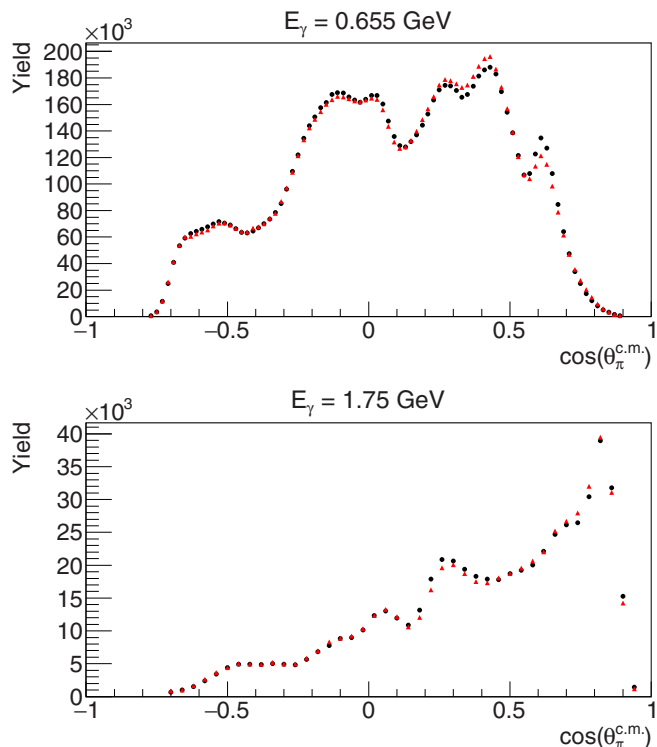
acceptance within each E_γ bin were rejected from the analysis. The CLAS acceptance of the $\gamma d \to \pi^- p(p)$ reaction for the CLAS g13 experiment after this cut is shown in Fig. 9 for selected beam energy bins. Overall, the acceptance varied between 5% and 50%, and the large dips were primarily due to triggering inefficiencies and drift chamber problem areas.

The systematic uncertainty due to event selection was typically less than 2%, although it increased to 10% near the edges of the detector. The uncertainty due to the yield extraction was less than 5%. These uncertainties were determined by varying the widths of the cuts used, and the range and starting parameters of the missing mass fits.

The systematic uncertainties due to the acceptance corrections were typically less than 5%, but increased to 10% in problematic regions with low triggering or drift chamber acceptance. These uncertainties were determined by studying how the acceptance-corrected yields changed when individual CLAS sectors and target vertex-z bins were removed from the analysis. A small number of bins had large ($\geqslant 5\%$) systematic uncertainties for half of the CLAS sectors, and were removed from the results. Overall, the angular-dependent systematic uncertainties varied between 1% and 15%.

VI. LUMINOSITY DETERMINATION

The number of tagged photons incident on the target while the data acquisition (DAQ) system was ready to record events,
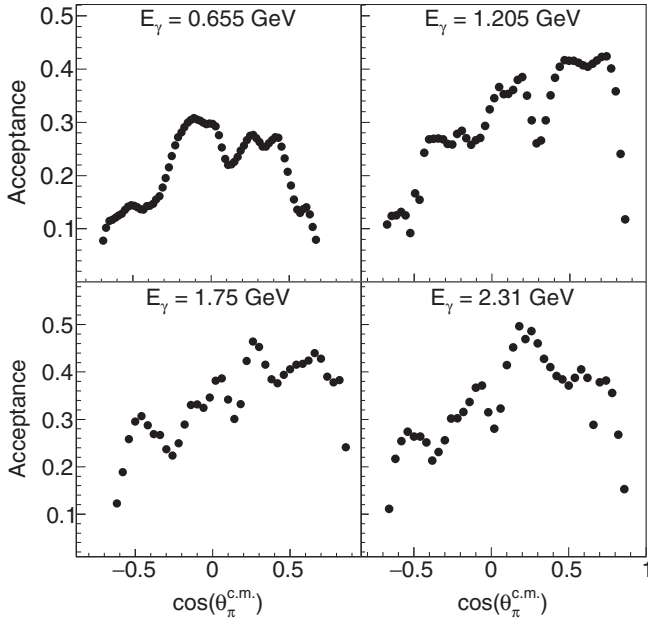
FIG. 9. The CLAS acceptance in selected energy bins as a function of the pion c.m. angle $\cos \theta_\pi^{c.m.}$. The dips in the acceptance are primarily due to triggering inefficiencies and problematic areas of the drift chambers.

N_γ, was calculated separately for each tagger counter as [20]:

$$N_\gamma = \epsilon N_e, \tag{2}$$

where ϵ is the tagging ratio of the given tagger counter and N_e is the number of detected electron hits in that counter while the DAQ was ready. N_e was calculated from the rate of "out-of-time" electron hits and the livetime of the DAQ. "Out-of-time" hits are from electrons that did not coincide in time with the trigger, and were used so that the rate calculation was not biased by the trigger.

The tagging ratios ϵ were determined by taking several normalization runs throughout the g13 experiment. During these runs, a total absorption counter (TAC) was inserted into the beamline to determine the number of photons incident on the target. The TAC was positioned about 25 m downstream of CLAS and consisted of a single lead-glass block. A PMT attached to the block was used to count the number of photons incident on the TAC, which was 100% efficient [11]. A low beam current of 0.1 nA was necessary to prevent radiation damage to the TAC during these normalization runs.

For each normalization run the tagging ratios were calculated for each tagger counter as [20]

$$\epsilon = \frac{N_{\mathrm{TAC}}}{N(1-\alpha)}, \tag{3}$$

where N is the total number of electron hits in a given tagger counter, N_{TAC} is the total number of these hits that represent coincident matched photon hits in the TAC for that tagger counter, and α is the photon attenuation factor. This factor takes into account the fraction of the photons incident on the target that did not reach the TAC. This photon attenuation factor was ~4% and was energy independent [21]. These

losses were primarily due to electron-positron pair production and Compton scattering as the photons interacted with the target and the beamline components. The tagging ratios were typically 60–72% for the 1.990-GeV data and between 73% and 82% for the 2.655-GeV data. Because the beam was collimated through a 6.4-mm opening, the tagging ratios were lower for the 1.990-GeV data due to the larger beam dispersion of the lower-energy beam.

In total, approximately 46.8 trillion tagged photons were incident on the CLAS target in this analysis. The statistical uncertainty on the flux measurement ranged between 0.0024% and 0.14%, and are reported as energy-dependent normalization uncertainties. The systematic uncertainty of the photon flux was determined by examining the stability of the flux-normalized yields of $\gamma d \to \pi^- p(p)$ throughout the experimental run. These systematic uncertainties were 0.4% and 0.7% for the 1.990- and 2.655-GeV data, respectively, and are reported as energy-independent normalization uncertainties.

In addition, the systematic uncertainties on the target length and density determinations were each 0.4%, and were dominated by thermal contraction and temperature variation, respectively. These uncertainties are reported as energy-independent normalization uncertainties.

VII. DIFFERENTIAL CROSS SECTIONS

The data from the 1.990- and 2.655-GeV electron beam energies were merged together to produce the final set of measured $\gamma d \to \pi^- p(p)$ differential cross sections. This merging was performed by calculating an uncertainty-weighted average of the two cross section measurements in bins where both were available. In bins where data were only available from one beam energy, only that result was used.

The differential cross section of the $\gamma d \to \pi^- p(p)$ reaction was calculated for each bin of photon beam energy E_γ and $\cos \theta_\pi^{c.m.}$ as

$$\frac{d\sigma}{d\Omega}\big(E_\gamma, \ \cos \theta_\pi^{c.m.}\big)$$
$$= \frac{1}{2\pi\big(\Delta \cos \theta_\pi^{c.m.}\big)} \frac{A_r}{\rho L N_A} \frac{Y\big(E_\gamma, \cos \theta_\pi^{c.m.}\big) Y_{\mathrm{CF}}}{\Phi(E_\gamma) A\big(E_\gamma, \cos \theta_\pi^{c.m.}\big)}, \tag{4}$$

where $\Delta \cos \theta_\pi^{c.m.}$ is the bin width in $\cos \theta_\pi^{c.m.}$, A_r is the effective atomic weight of the neutrons in the deuterium target, ρ is the target density, L is the target length, N_A is Avogadro's number, Φ is the photon flux in the given photon energy bin, Y is the experimental yield in the given bin, A is the simulated acceptance in the given bin, and Y_{CF} is the yield correction factor discussed in Sec. V. The factor of 2π is due to the integration over the azimuthal angle ϕ in the binning used for the cross section calculation. The statistical uncertainty of the cross section was calculated for each bin by combining the statistical uncertainties of the experimental yield and simulated acceptance in quadrature, and ranged between 0.3% and 5%. These uncertainties were dominated by the yield uncertainties. All data from this measurement are included in the CLAS physics database [22].

To study the stability of the overall normalization of the $\gamma d \rightarrow \pi^- p(p)$ cross section measurements, it was calculated separately for several different run ranges throughout both beam energy settings of the experiment. Overall, the total spread between the measurements was 2.4%, and is reported as an energy-independent normalization uncertainty. This uncertainty takes into account any systematic differences between the 1.990- and 2.655-GeV data that were merged together. The total normalization uncertainties were about 3.4%, and were primarily due to this run range-dependent variation in the cross section measurements and the FSI corrections, which are discussed in Sec. VIII. The total uncertainty on the $\gamma d \rightarrow \pi^- p(p)$ cross sections is typically between 4.2% and 15%.

To extract the $\gamma n \rightarrow \pi^- p$ differential cross sections, model-dependent final state interaction corrections were applied to the $\gamma d \rightarrow \pi^- p(p)$ data, as discussed in Sec. VIII. These data were split up into 157 photon energy bins from 0.440 to 2.520 GeV, 10 MeV wide below 1.5 GeV and 20 MeV wide above. The $\gamma n \rightarrow \pi^- p$ differential cross section measurements are shown for 40 of these E_γ bins in Figs. 10 and 11, compared against previous measurements and available partial wave analysis solutions. They are also shown in Fig. 12 vs W in four bins of $\cos\theta_\pi^{c.m.}$. These figures include $\gamma n \rightarrow \pi^- p$ measurements from CLAS g10 [8], SLAC [23], DESY [24], MAMI-B [25], and Frascati [26], and $\pi^- p \rightarrow \gamma n$ measurements from BNL [27], LBL [28], and LAMPF [29]. Only the angle-dependent uncertainties are shown for all measurements. All non-CLAS g13 data shown in Figs. 10 and 11 are within ± 10 MeV of the selected g13 energy bin, and all non-CLAS g13 data shown in Fig. 12 are within $\cos\theta_\pi^{c.m.}$ of ± 0.05 of the g13 angle bin.

The differential cross section peaks at low energy due to $\Delta(1232)$ and N^* resonance production, and at forward angles due to t-channel pion exchange. Below $E_\gamma = 1$ GeV, the new CLAS g13 data dominate the previous world measurements, with $\cos\theta_\pi^{c.m.}$ bins 0.02 wide and total uncertainties typically less than 10% in this range. The CLAS g13 data are systematically lower than the DESY [24], BNL [27], and SLAC [23] measurements in several energy bins, and each of these measurements quote normalization uncertainties of about 5%. There is also a discrepancy in the trend of the data at forward angles between the CLAS g13 and SLAC measurements below $E_\gamma = 0.800$ GeV, with the g13 data rising more sharply at forward angles.

Above $E_\gamma = 1$ GeV, the g13 data are reported in bins that are 0.03 wide in $\cos\theta_\pi^{c.m.}$ up to 1.5 GeV, and 0.04 wide in $\cos\theta_\pi^{c.m.}$ above 1.5 GeV. Here, the CLAS g10 data [8] were the previous highest-statistics measurement, reported in 50- and 100-MeV-wide beam energy bins. The g13 data are in excellent agreement with these measurements, as the g10 data have normalization uncertainties of $\sim$6% to $\sim$10% that are not shown in the figures.

The SAID PR15 [30], Bonn-Gatchina BG2014-02 [4], and MAID2007 [31] curves shown in these figures did not include the new CLAS g13 data in their fits, and the MAID2007 fit does not include the CLAS g10 measurements either. The data in these previous fits, and in the new SAID MA27 fit that includes the g13 data, are discussed in Sec. X.

VIII. FINAL STATE INTERACTIONS

The $\gamma n \rightarrow \pi^- p$ cross sections were extracted on a free neutron from the deuteron data in the quasifree kinematic region of the $\gamma d \rightarrow \pi^- pp$ reaction, which has a fast knocked-out proton p_1 and a slow proton spectator p_2, assumed not to be involved in the pion production process. In this quasifree region, the reaction mechanism corresponds to the "dominant" impulse approximation (IA) diagram in Fig. 13(a) with the slow proton p_2 emerging from the deuteron vertex. Here, the differential cross section on the deuteron can be related to that on the neutron target in a well understood way [see, e.g., Eq. (22) of Ref. [32] and references therein]. Figure 13(a) illustrates this dominant IA diagram, as well as the "suppressed" IA diagram with the protons interchanged. This approximation, with the additional assumption that the neutron is at rest in the deuteron, allows for the identification of the quasifree cross section $\frac{d\sigma}{d\Omega}$ on the deuteron with that on the neutron, where $d\Omega$ is the solid angle of the outgoing pion in the γn rest frame. The γn cross section can be calculated as

$$\frac{d\sigma}{d\Omega}(\gamma n) = R\left(E_\gamma, \theta_\pi^{c.m.}\right)^{-1}\frac{d\sigma}{d\Omega}(\gamma d), \qquad (5)$$

where $\frac{d\sigma}{d\Omega}(\gamma d)$ is the quasifree CLAS g13 measurement on the deuteron and $R(E_\gamma, \theta_\pi^{c.m.})$ is the FSI correction factor that takes into account the FSI effects discussed below, as well as the identity of the two protons in the γd reaction. This factor is defined as the ratio between the full contribution of the three diagrams in Fig. 13 and that of the dominant IA diagram in Fig. 13(a). There are two critical factors to consider when using this approach: (1) the neutron is bound in the deuteron and not at rest, and (2) there are NN- and πN-FSI effects.

Factor (1) means that the effective mass of the neutron,

$$m_{\rm eff} = \sqrt{(p_d - p_s)^2} \approx m_n - \epsilon_d - \vec{p}_s^{\,2}/m_N, \qquad (6)$$

is not equal to the mass of the free neutron m_n. Here, p_d, p_s, $\vec{p}_s$, ϵ_d, and m_N are the deuteron four-momentum, four- and three-momenta of the spectator proton, the deuteron binding energy, and the nucleon mass, respectively. Also, the invariant mass $\sqrt{s_{\pi N}}$ of the final πN system,

$$\sqrt{s_{\pi N}} = \sqrt{s_{\gamma N}} = \sqrt{[(E_\gamma + m_d - E_s)^2 - (\vec{p}_\gamma - \vec{p}_s)^2]}, \quad (7)$$

depends on the proton-spectator momentum $\vec{p}_s$ ($s_{\gamma N}$ is the invariant mass squared of the initial γN state). Here, E_γ (E_s), m_d, and $\vec{p}_\gamma$ are the total energy of the initial photon (proton-spectator), the deuteron mass, and the photon three-momentum, respectively, and $E_\gamma = |\vec{p}_\gamma|$.

Since $\sqrt{s_{\pi N}}$ depends on $\vec{p}_s$, the $\gamma N \rightarrow \pi N$ cross section extracted from the deuteron data, with an undetected nucleon spectator, is averaged over an energy range that depends on the kinematic cuts employed for $\vec{p}_s$. Thus, the effective photon laboratory energy $E_{\gamma n}$ (defined through the relation $s_{\gamma N} = m_n^2 + 2m_n E_{\gamma n}$ for the $\gamma n \rightarrow \pi^- p$ reaction) and the pion c.m. angle $\theta_\pi^{c.m.}$ are smeared due to the deuteron wave function (DWF). This smearing has been estimated from a simplified calculation, where the $\gamma d \rightarrow \pi^- pp$ amplitude is proportional to the DWF and depends only on the laboratory momentum of one of the final protons, say p_2. Here, $E_{\gamma n}$ is determined
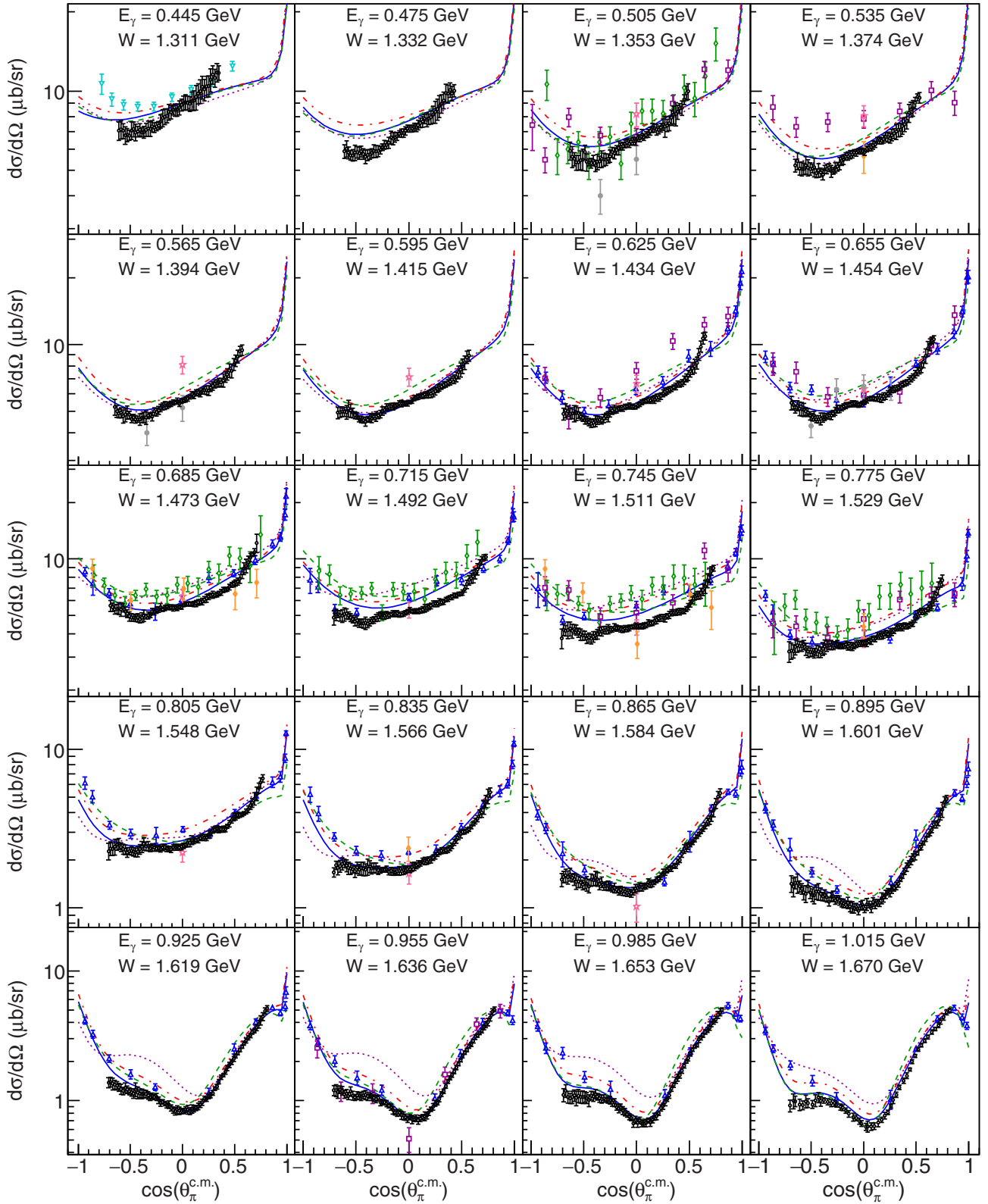
FIG. 10. Selected cross section data for $\gamma n \to \pi^- p$ vs $\cos\theta_\pi^{c.m.}$ below $E_\gamma = 1.05$ GeV: CLAS g13 (black open circles), SLAC [23] (blue open triangles), DESY [24] (violet open squares), MAMI-B [25] (cyan open down triangles), and Frascati [26] (pink open stars); $\pi^- p \to \gamma n$ data: BNL [27] (green open diamonds), LBL [28] (orange closed diamonds), and LAMPF [29] (gray closed circles); fits: SAID MA27 (blue solid lines), SAID PR15 [30] (red dot-dashed lines), BG2014-02 [4] (green dashed lines), and MAID2007 [31] (violet dotted lines). The y axes are log scale. Only angle-dependent uncertainties are shown for all data. The total normalization uncertainties for the CLAS g13 data are about 3.4%.
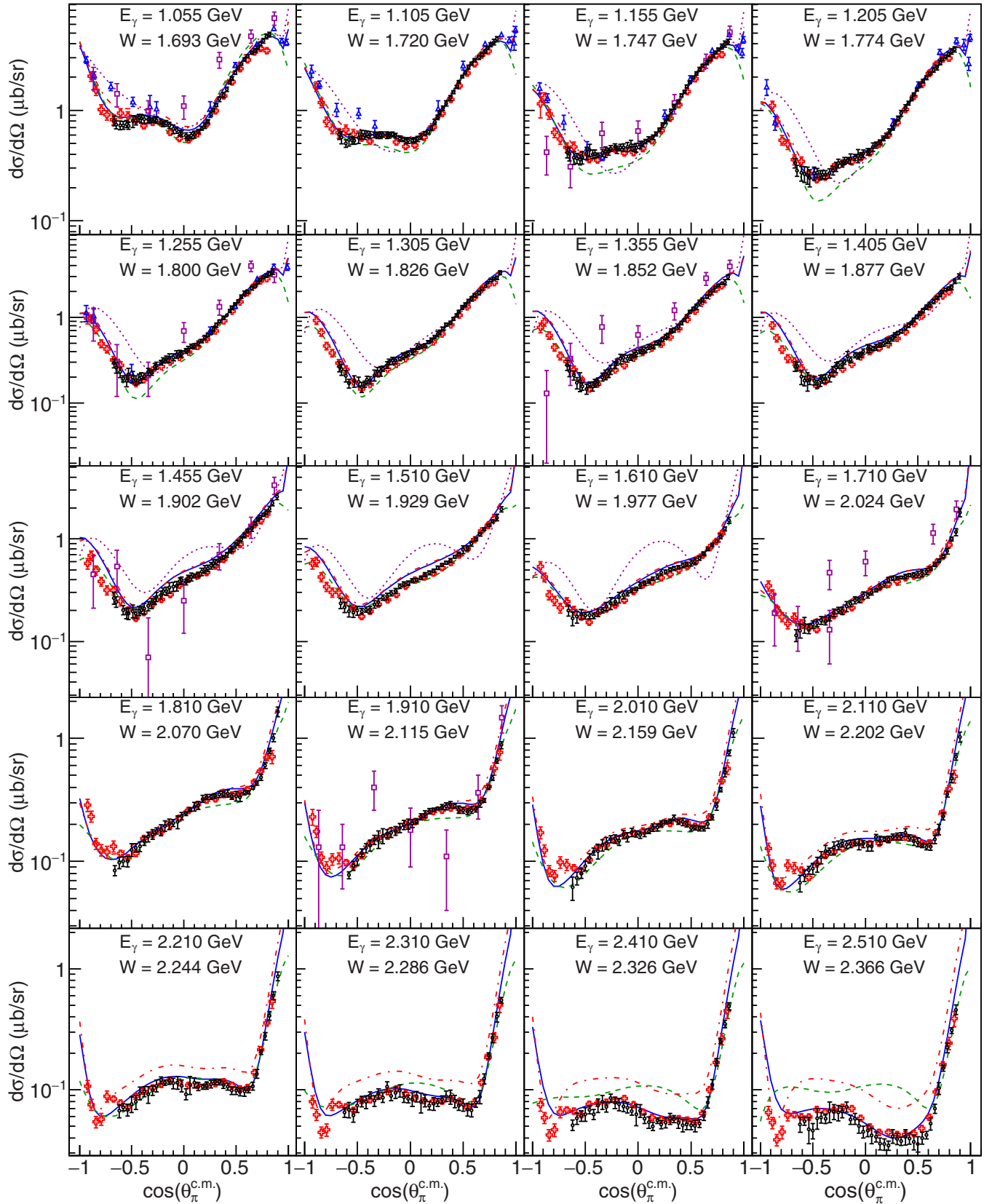
FIG. 11. Selected cross section data for $\gamma n \to \pi^- p$ vs $\cos\theta_\pi^{c.m.}$ above $E_\gamma = 1.05$ GeV: CLAS g13 (black open circles), CLAS g10 [8] (red open pluses), SLAC [23] (blue open triangles), and DESY [24] (violet open squares); fits: SAID MA27 (blue solid lines), SAID PR15 [30] (red dot-dashed lines), BG2014-02 [4] (green dashed lines), and MAID2007 [31] (violet dashed lines). The y axes are log scale. Only angle-dependent uncertainties are shown for all data. The total normalization uncertainties for the CLAS g13 data are about 3.4%.
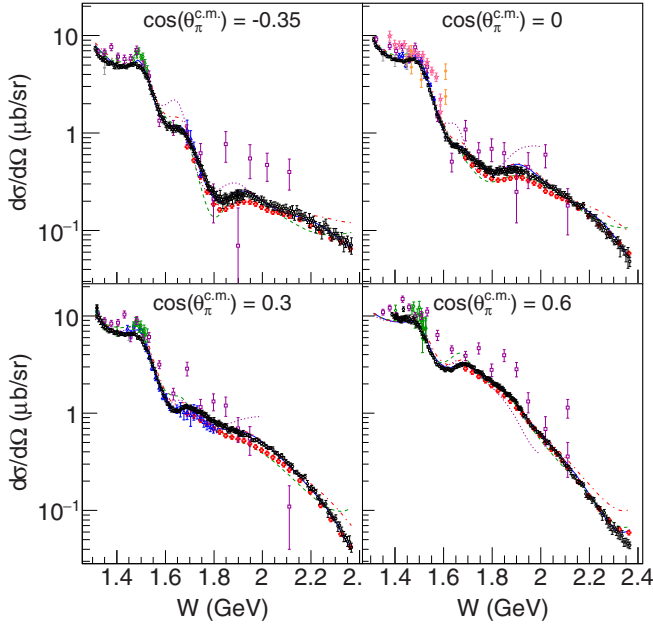
FIG. 12. Selected cross section data for $\gamma n \to \pi^- p$ vs W: CLAS g13 (black open circles), CLAS g10 [8] (red open pluses), SLAC [23] (blue open triangles), DESY [24] (violet open squares), MAMI-B [25] (cyan open down-triangles), and Frascati [26] (pink open stars); $\pi^- p \to \gamma n$ data: BNL [27] (green open diamonds), LBL [28] (orange closed diamonds), and LAMPF [29] (gray closed circles); fits: SAID MA27 (blue solid lines), SAID PR15 [30] (red dot-dashed lines), BG2014-02 [4] (green dashed lines), and MAID2007 [31] (which terminates at $W = 2$ GeV or $E_\gamma = 1.65$ GeV) (violet dotted lines). The y axes are log scale. Only angle-dependent uncertainties are shown for all data. The total normalization uncertainties for the CLAS g13 data are about 3.4%.

through the above-mentioned relation with the effective mass of the pion-proton pair with the other proton p_1. The distortion of the extracted $\gamma n \to \pi^- p$ cross sections due to the smearing effect is negligible, as was shown in Ref. [25].

Factor (2) corresponds to the inclusion of the FSI corrections. Their leading terms correspond to the Feynman diagrams shown in Figs. 13(b) and 13(c). The GWU SAID database contains phenomenological amplitudes for the reactions $\pi N \to \pi N$ [33], $NN \to NN$ [34], and $\gamma N \to \pi N$ [35], which were used as inputs to calculate the dominant
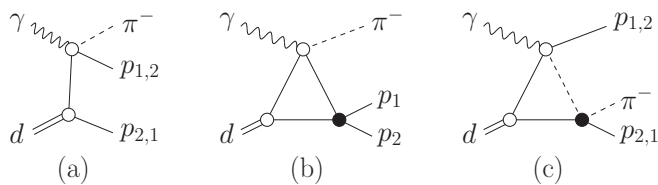

FIG. 13. Feynman diagrams for the leading terms of the $\gamma d \to \pi^- pp$ amplitude: (a) IA, (b) pp-FSI, and (c) πN-FSI. The filled black circles represent the FSI vertices. The wavy, dashed, solid, and double lines correspond to the photons, pions, nucleons, and deuterons, respectively.

diagrams of the GWU-ITEP FSI approach. The full Bonn potential [36] was used for the deuteron description.

Calculations of the $\gamma d \to \pi^- pp$ differential cross sections with the FSI taken into account (including all diagrams in Fig. 13) were done for the present g13 data as they were done previously for the CLAS g10 data ($E_\gamma = 1.050$ to 2.700 GeV and $\theta_\pi^{c.m.} = 32°$ to $157°$) [8] and MAMI-B data ($E_\gamma = 0.301$ to 0.455 GeV and $\theta_\pi^{c.m.} = 58°$ to $141°$) [25].

The GWU-ITEP FSI calculations [32] are available over a broad energy range (threshold to $E_\gamma = 2.700$ GeV) and for the full c.m. angular range ($\theta_\pi^{c.m.} = 0°$ to $180°$). Figure 14 shows the FSI correction factor $R = R(E_\gamma, \theta_\pi^{c.m.})$ for the $\gamma n \to \pi^- p$ differential cross section as a function of $\theta_\pi^{c.m.}$ for different energies over the range of the CLAS g13 experiment. Overall, the FSI correction factor $R < 1$, while the value of R varied from 70% to 90% depending on the kinematics. The behavior of R is very smooth vs pion production angle. Note that $R(E_\gamma, \theta_\pi^{c.m.})$ is the FSI correction factor for the CLAS quasifree $\gamma d \to \pi^- pp$ cross section averaged over the laboratory photon energy E_γ bin width.

The contribution of FSI calculations [32] to the overall systematic normalization uncertainty is estimated to be about 2.2% (the sensitivity to the DWF is 1% and to the number of steps in the integration of the fivefold integrals is 2%). No sensitivity was found to the kinematic cuts used for the detected protons in CLAS.

IX. LEGENDRE ANALYSIS

Legendre expansions provide a model-independent approach suitable for presentation of modern detailed (high-precision, high-statistics, and narrow energy and angular binning) data for pion photoproduction reactions [37]. This approach is applicable both to cross sections and to polarization observables; it is much more compact and visual than traditional methods (see, for instance, Figs. 10–12), at least at energies within the nucleon resonance region. The Legendre coefficients reveal specific correlations and interferences between resonant states of definite parities.

The small statistical uncertainties of the g13 data obtained here allow a correspondingly robust determination of the Legendre polynomial coefficients $A_J(W)$. These coefficients were very difficult to determine unambiguously with previously published π^- photoproduction data of lower statistical accuracy. Because of the limited angular range of the g13 data, several sets of quasidata were generated using the MA27 SAID solution (see Sec. X for details) in bins with width $\Delta \cos \theta_\pi^{c.m.} = 0.05$ for the forward and backward directions to cover the full angular range.

It is important to note that the MA27 solution was constrained at the forward and backward angular ranges beyond the extent of the g13 data by the existing world data shown in Figs. 10–12. However, as the available data do not span the full $\cos \theta_\pi^{c.m.}$ range for the W range of the g13 data, the MA27 quasidata were conservatively assigned 10% uncertainties, which matches the largest of the experimental uncertainties reported within the g13 data, excepting a few regions with a problematic acceptance determination. Conser-
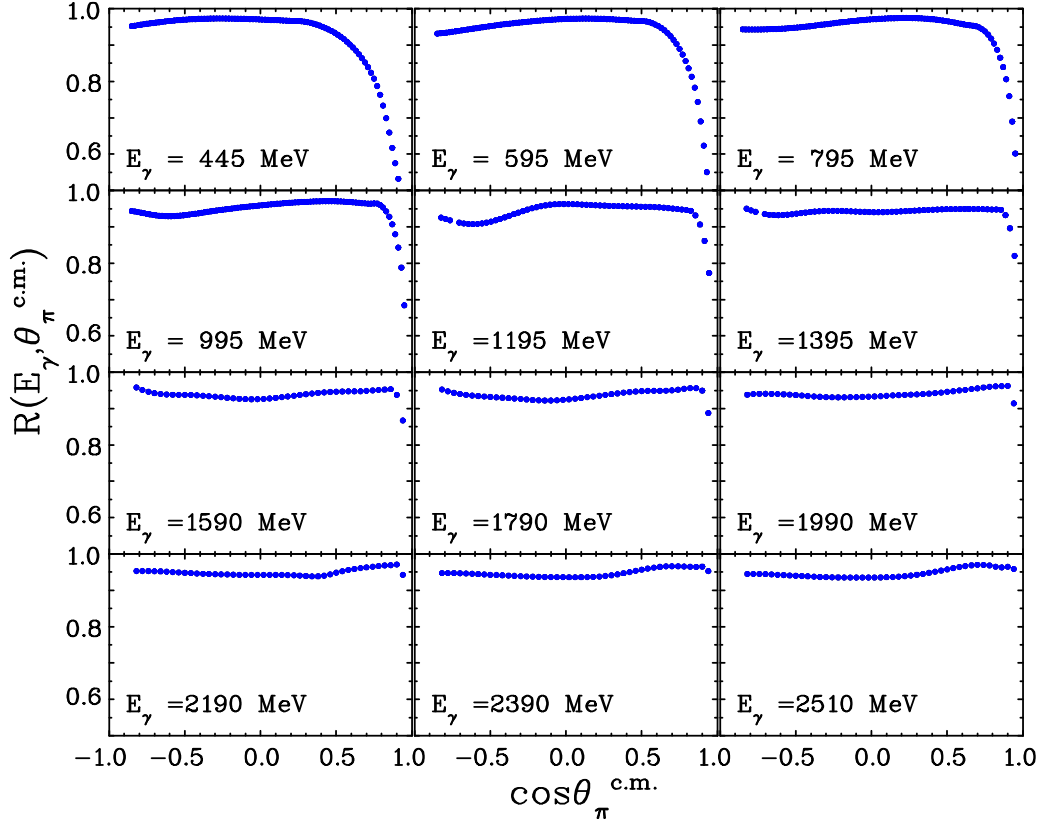
FIG. 14. The FSI correction factor $R(E_\gamma, \theta_\pi^{c.m.})$ for selected beam energies vs $\cos \theta_\pi^{c.m.}$, where $\theta_\pi^{c.m.}$ is the polar angle of the outgoing π^- in the rest frame of the π^- and the fast proton. The fast knocked-out protons p_1 with momentum $>200\,\text{MeV}/c$ were selected, while the slow proton spectators p_2 have momentum $<200\,\text{MeV}/c$. The 2% normalization uncertainties are not shown.

vative assignment of uncertainties in these regions is important as these regions are quite sensitive to the highest partial waves.

As expected for such a fit using orthogonal polynomials, the Legendre coefficients $A_J(W)$ decrease markedly for large J. With the energy range and precision of the g13 data, a maximum value of $J = 10$ was found to be sufficient to describe the data (similar to the analysis of the CLAS π^0 and $\pi^+ \Sigma$ beam asymmetry measurements [38]). Thus, the infinite series is truncated as

$$\frac{d\sigma\left(W, \cos\theta_\pi^{c.m.}\right)}{d\Omega} = \sum_{J=0}^{10} A_J(W)\, P_J\left(\cos\theta_\pi^{c.m.}\right), \quad (8)$$

where the total cross section $\sigma^{\text{tot}} = 4\pi A_0(W)$.

In Fig. 15, the Legendre coefficients $A_0(W)$ to $A_{10}(W)$ are shown as a function of W from the fit of the CLAS g13 $d\sigma/d\Omega$ data and the $d\sigma/d\Omega$ data generated from the MA27 predictions. The individual Legendre coefficients have been scaled by $n \times A_J + m$ to allow plotting on a common abscissa. The n and m scaling values are given in the subplots of Fig. 15.

The results of our fits yield unprecedented detail on the energy dependence of the Legendre coefficients $A_J(W)$, and should prove useful for performing a phase shift analysis of pion photoproduction data for the present energy range. As expected from the form of Eq. (28) of Ref. [37], resonance contributions from the second, third, and fourth resonance regions combine to produce clear peaks in the coefficient

$A_0(W)$. It is interesting that all $A_J(W)$ coefficients show structure for the $W = 1.3$ to 1.8 GeV range, which was also seen in the MAMI A2 π^0 data [30]. However, wide structures are also visible in the range $W = 1.8$ to 2.0 GeV, most likely attributable to contributions from one or more nucleon resonances known in this energy range with spin up to 7/2, as was seen in the recent CLAS g8 π^0 and $\pi^+ \Sigma$ beam asymmetry measurement Legendre analysis [38].

The Legendre fit results shown in Fig. 15 do not include any assignment of model uncertainties associated with the extrapolations of the MA27 model beyond the range of the available data. Such assignments could be expected to be non-negligible for the higher Legendre moments shown here. However, our purpose in displaying the Legendre fit results is not to perform a quantitative amplitude analysis, but to showcase how the precision g13 cross section measurements can provide significant constraints on the resonance contributions over a broad range in W.

X. MULTIPOLE ANALYSIS

The SAID parametrization of the transition amplitude $T_{\alpha\beta}$ used in the hadronic fits to the πN scattering data is given as

$$T_{\alpha\beta} = \sum_\sigma [1 - \overline{K}C]^{-1}_{\alpha\sigma} \overline{K}_{\sigma\beta}, \quad (9)$$
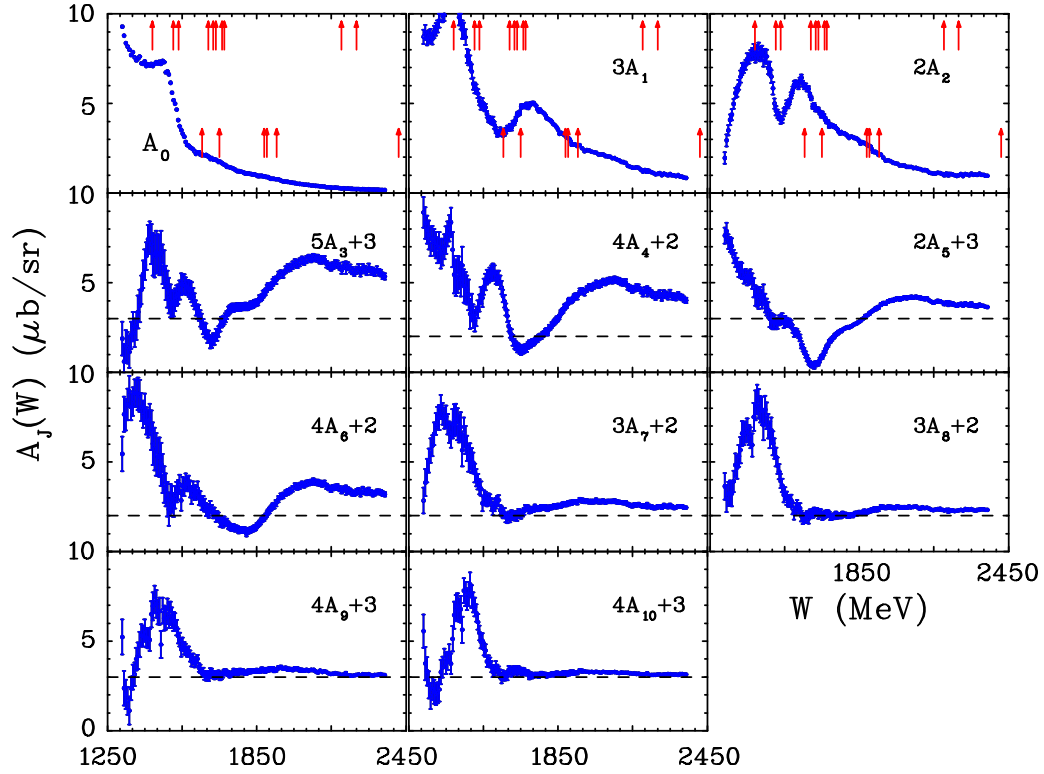
FIG. 15. Coefficients of the Legendre polynomials $A_J(W)$ (blue filled circles) from the fits of the CLAS g13 $\gamma n \rightarrow \pi^- p$ cross section data. The error bars represent the $A_J(W)$ uncertainties from the fits in which only the statistical uncertainties were used. The $A_J(W)$ coefficients have been scaled (dashed horizontal lines) by $n \times A_J + m$ to enable easy visualization. The red vertical arrows in the top row of plots indicate the masses of the PDG four-star resonances (Breit-Wigner masses) in this energy range [2]. The upper row of arrows corresponds to N^* states with isospin $I = 1/2$ and the lower row corresponds to Δ^* states with $I = 3/2$.

where α, β, and σ are channel indices for the πN, $\pi \Delta$, ρN, and ηN channels. Here $\overline{K}_{\alpha\beta}$ are the Chew-Mandelstam K matrices, which are parametrized as polynomials in the scattering energy. C_α is the Chew-Mandelstam function, an element of a diagonal matrix C in channel space, which is expressed as a dispersion integral with an imaginary part equal to the two-body phase space [39].

In Ref. [40], it was shown that this form could be extended to $T_{\alpha\gamma}$ to include the electromagnetic channel as

$$T_{\alpha\gamma} = \sum_\sigma [1 - \overline{K}C]^{-1}_{\alpha\sigma} \overline{K}_{\sigma\gamma}. \qquad (10)$$

Here, the Chew-Mandelstam K-matrix elements associated with the hadronic channels are kept fixed from the previous SAID solution SP06 [33], and only the electromagnetic elements are varied. The resonance pole and cut structures are also fixed from hadronic scattering. This provides a minimal description of the photoproduction process, where only the N^* and Δ^* states present in the SAID πN scattering amplitudes are included in this multipole analysis.

For each angular distribution, a normalization constant (X) and its uncertainty (ϵ_X) were assigned. The quantity ϵ_X is generally associated with the normalization uncertainty (if known). The modified χ^2 function to be minimized

is given by

$$\chi^2 = \sum_i \left(\frac{X\theta_i - \theta_i^{\mathrm{exp}}}{\epsilon_i} \right)^2 + \left(\frac{X - 1}{\epsilon_X} \right)^2, \qquad (11)$$

where the subscript i labels the data points within the distribution, θ_i^{exp} is an individual measurement, θ_i is the corresponding calculated value, and ϵ_i represents the total angle-dependent uncertainty. The total χ^2 is then found by summing over all measurements. This renormalization freedom is essential for obtaining the best SAID fit results. For other data analyzed in the fit, such as the total cross sections and excitation data, the statistical and systematic uncertainties were combined in quadrature and no renormalization was allowed.

In the previous fits to the $\gamma n \rightarrow \pi^- p$ differential cross sections of Ref. [8], the unrestricted best fit gave renormalization constants X significantly different from unity. As can be seen from Eq. (11), if an angular distribution contains many measurements with small statistical uncertainties, a change in the renormalization may improve the fit with only a modest χ^2 penalty. Here, however, the weight of the second term in Eq. (11) has been adjusted by the fit for each dataset to keep the renormalization constants approximately within ϵ_X of unity. This was possible without degrading the overall fit χ^2, as can be seen in Fig. 16.
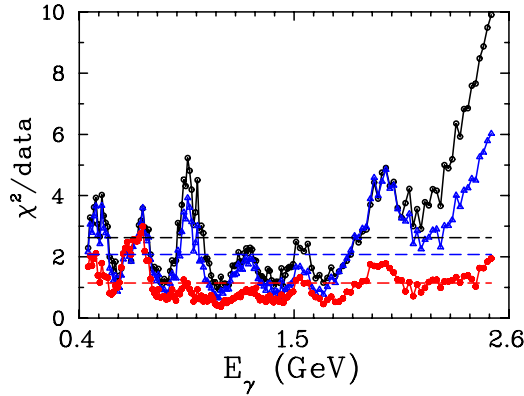
FIG. 16. Comparison of the previous SAID solution PR15 [30] applied to the present g13 data with (blue filled triangles) and without FSI corrections (black open circles), and the new SAID MA27 (red full circles) solution obtained after adding the present g13 data with FSI corrections into the fit (the solid lines connecting the points are included only to guide the eye). Shown are the fit χ^2 per data point values averaged within each energy bin E_γ, where the horizontal dashed lines (blue (black) for PR15 and red for MA27) show the overall χ^2 per data point values from Table II.

With the new high-precision $\gamma n \rightarrow \pi^- p$ cross sections from the CLAS g13 dataset, a new SAID multipole analysis has been completed. This new global energy-dependent solution has been labeled as MA27. The overall fit quality of the present MA27 and previous SAID PR15 solutions are compared in Tables I and II. The inclusion of the g13 dataset shows significant improvement in the comparisons between the $\pi^- p$ fits and data ($\chi^2/d.p.$ for PR15 = 2.08 and $\chi^2/d.p.$ for MA27 = 1.10) as shown in Fig. 16 and Table I. This demonstrates the power of these cross section measurements with their small uncertainties. The overall comparison of the PR15 and MA27 solutions in Table II shows that the fit $\chi^2/d.p.$ values are essentially unchanged for the $\pi^0 p$ and $\pi^+ n$ channels but are notably worse for the $\pi^0 n$ channel, which has very low statistics. The overall χ^2 per data point including all available data and the new g13 data for PR15 is $\chi^2/d.p. = 2.19\,(103\,747/47\,353)$ and for MA27 is $\chi^2/d.p. = 1.99\,(94\,248/47\,353)$.

TABLE I. Comparison of χ^2 per data point $(d.p.)$ below $E_\gamma = 2.7$ GeV ($W = 2.5$ GeV) for the $\gamma n \rightarrow \pi^- p$ channel using predictions for the recent SAID PR15 [30] and the current MA27 solution. The first row of solutions compares the fit quality to the available data not including the CLAS g13 data. The second row compares the solutions to the available data including the g13 data. The last row compares the solutions only to the g13 data.

Data	Solution	$\chi^2/(\pi^- p\, d.p.)$
Existing data	PR15	$6541/3162 = 2.07$
without g13	MA27	$7112/3162 = 2.25$
Existing data	PR15	$24052/11590 = 2.08$
with g13	MA27	$16442/11590 = 1.42$
Only	PR15	$17511/8452 = 2.07$
g13	MA27	$9330/8452 = 1.10$

In Figs. 17–19, $I = 1/2$ multipole amplitudes from the present and previous SAID fits are compared to predictions from the MAID and Bonn-Gatchina groups. The Bonn-Gatchina analysis has been regularly updated, whereas the MAID fit was published in 2007 and therefore does not include any results from the past decade, including the recent CLAS g10 cross section measurements of Ref. [8]. The cross section requires $I = 3/2$ multipoles as well, but these are highly constrained by proton-target measurements and have not changed significantly with the addition of neutron-target measurements (and therefore are not shown here). In the multipole plots, the subscript n denotes a neutron target and $\ell\pm$ gives the value of $j = \ell \pm 1/2$, while the superscript gives the isospin index.

Changes in the multipole amplitudes can be seen in a comparison of the SAID curves in Figs. 17–19. Consistency among the analyses is visible in multipoles containing a dominant resonance, such as the $_nE_{2-}^{1/2}$ and $_nM_{2+}^{1/2}$ multipoles. However, the $_nE_{1+}^{1/2}$ and $_nM_{1+}^{1/2}$ multipoles differ even at the qualitative level. This discrepancy is evident in the proton-target multipoles as well.

The full world database of $\gamma n \rightarrow \pi^- p$ experiments above $E_\gamma = 1.2$ GeV contains mainly differential cross sections, apart from some Σ beam asymmetry measurements from Yerevan [41], GRAAL [42], and CEA [43]. Ultimately, more measurements of the polarization observables are needed in the $\pi^- p$ and $\pi^0 n$ channels in order to fully constrain the underlying reaction amplitudes. New γn measurements from the CLAS g14 dataset [44] will significantly add to the available polarization observable measurements.

Looking for significant changes in the imaginary parts of the multipoles (Figs. 17–19) in the energy region below the older set of CLAS g10 cross sections [8], several $N^* \rightarrow \gamma n$ photodecay amplitudes have been extracted at their pole positions on the complex plane. This is the first determination of these amplitudes for the $N(1440)1/2^+$, $N(1535)1/2^-$, $N(1650)1/2^-$, and $N(1720)3/2^+$ states. A new approach has been applied to determine the pole positions and residues from the pion photoproduction multipoles [45]. The method is based on a Laurent expansion of the multipoles, $M(W)$, with a Pietarinen series representing the regular (nonpole) part of the energy dependence as

$$M(W) = \sum_{i=1}^{k} \frac{a_{-1}^{(i)}}{W - W_i} + B^L(W). \qquad (12)$$

Here W, $a_{-1}^{(i)}$, and W_i are complex numbers representing the c.m. energy, residues, and pole positions for the ith pole, respectively, and $B^L(W)$ is a regular function in the whole complex plane. A general unknown analytic function $B(W)$ can be expanded into a power series of Pietarinen functions as

$$B^L(W) = \sum_{n=0}^{M} c_n\, X(W)^n + \sum_{n=0}^{N} d_n\, Y(W)^n$$

$$+ \sum_{n=0}^{N} e_n\, Z(W)^n + \cdots,$$

TABLE II. Comparison of χ^2 per data point ($d.p.$) below $E_\gamma = 2.7$ GeV ($W = 2.5$ GeV) for all $\gamma N \to \pi N$ channels using predictions for the recent SAID PR15 [30] and the current MA27 solution. The fit quality for the $\pi^0 p$, $\pi^+ n$, $\pi^- p$, and $\pi^0 n$ channels is compared to the available data including the g13 data.

Data	Solution	$\chi^2/(\pi^0 p\ d.p.)$	$\chi^2/(\pi^+ n\ d.p.)$	$\chi^2/(\pi^- p\ d.p.)$	$\chi^2/(\pi^0 n\ d.p.)$
Existing data	PR15	$54\,985/25\,540 = 2.15$	$23\,558/9859 = 2.39$	$24\,052/11\,590 = 2.08$	$1152/364 = 3.16$
with g13	MA27	$55\,530/25\,540 = 2.17$	$20\,736/9859 = 2.10$	$16\,442/11\,590 = 1.42$	$1540/364 = 4.23$

$$X(W) = \frac{\alpha - \sqrt{x_P - W}}{\alpha + \sqrt{x_P - W}},$$

$$Y(W) = \frac{\beta - \sqrt{x_Q - W}}{\beta + \sqrt{x_Q - W}},$$

$$Z(W) = \frac{\gamma - \sqrt{x_R - W}}{\gamma + \sqrt{x_R - W}}, \tag{13}$$

where c_n, d_n, e_n and α, β, γ are real numbers that represent tuning parameters and coefficients of the Pietarinen functions $X(W)$, $Y(W)$, and $Z(W)$, respectively. A variable number of series was used, depending on the structure of the nonpole part of each amplitude, and x_P, x_Q, and x_R represent the branch points for each Pietarinen function. Once the pole position and residue were determined, the photodecay amplitude at the pole could be constructed, as described in Ref. [46]. The residue of the corresponding πN elastic scattering amplitude, required in this construction, was taken from the SAID analysis of elastic scattering data [33].

The $A_{1/2}(n)$ and $A_{3/2}(n)$ neutron helicity amplitudes for $N(1440)1/2^+$, $N(1535)1/2^-$, $N(1650)1/2^-$, and $N(1720)3/2^+$ for the new SAID MA27 solution are compared in Table III to the recent SAID GB12 [8] and BG2013 [47] solutions that were based on fits to all available data at the time, including the CLAS g10 dataset [8]. From this table, the photodecay amplitudes determined from the MA27 solution can be directly compared against the Breit-Wigner determinations. In addition, Table III includes a comparison to the older MAID2007 [31] solution, to the relativized quark model predictions of Ref. [48], and to the current PDG values [2]. The uncertainties on the modulus and phase quoted in Table III for the new MA27 solution were derived by comparing the global energy-dependent and energy-independent, single-energy amplitudes (see Ref. [49] for a discussion on the two approaches). The comparison gave residues with uncertainties. Extracting the photodecay amplitudes and considering the spread of possible values gave the MA27 uncertainties. These comparisons showed that the parameters from the MA27 solution are reasonably well under control.

The pole-valued and Breit-Wigner amplitudes from the fits are generally consistent in terms of the moduli. The comparisons are reasonable for the $N(1440)1/2^+$ and the $N(1535)1/2^-$. For the $N(1650)1/2^-$, the change from GB12 [8] is significant and the result is in reasonable agreement with BG2013 [47], which used the FSI corrected g10 $\gamma n \to \pi^- p$ cross sections that were used for GB12. The $N(1650)1/2^-$ state has been difficult to describe as it is so close to the $N(1535)1/2^-$ and the ηN cusp, however, this pole-valued determination is believed to be more model independent than

the Breit-Wigner amplitude [45], which is reflected in the quoted uncertainties shown in Table III. For the $N(1720)3/2^+$, the differences with respect to the BG2013 solution [47] are significant and indicate that the CLAS g13 data provide tighter constraints in the coupled-channel model fits.

Comparing the new SAID MA27 solution with the relativized quark model predictions of Ref. [48], there are significant differences in the helicity amplitudes for the $N(1440)1/2^+$ and $N(1650)1/2^-$, while the helicity amplitudes for the $N(1535)1/2^-$ and $N(1720)3/2^+$ are in good agreement. With respect to the current PDG values [2], Table III shows good correspondence with the MA27 solution for $N(1440)1/2^+$ and $N(1535)1/2^-$, but sizable disagreements for the higher-lying states.

A direct comparison of the quoted uncertainties on the neutron helicity amplitudes from the different solutions presented in Table III must be made with some caution. For the MA27, GB12, and BG2013 listings, the uncertainties do not take into account the significant model dependence in fitting the sparse database. In fact, the variance of the extracted results from different solutions fitting the same database would provide a reasonable estimate for this model dependence. However, this direct comparison is not possible given the different data sets employed for the different solutions shown in Table III. Considering this issue, it is still meaningful that the overall quoted uncertainties for the helicity amplitudes from the MA27 solution are noticeably reduced relative to the BG2013 solution and to the GB12 solution [in particular for the $N(1650)1/2^-$] due to a combination of two factors. The first is the increased size of the database for MA27 that includes the new g13 γn cross sections and the second is the reduced model dependence of the pole fit approach employed for MA27.

XI. SUMMARY AND CONCLUSIONS

A comprehensive set of $\gamma n \to \pi^- p$ differential cross sections at 157 photon energies has been determined with CLAS using a tagged-photon beam at incident photon energies from 0.445 to 2.510 GeV. These data provide a factor of nearly 3 increase to the world's data for this channel at these energies. To extract the γn cross section from the γd data, FSI corrections were included using a diagrammatic technique that takes into account a kinematic cut with momenta below (above) 200 MeV/c to select slow (fast) outgoing protons. In this analysis, the FSI correction factor depended on the photon energy and meson production angle, and was averaged over the rest of the variables in the region of the quasifree process on the neutron.

The data collected in this CLAS g13 dataset spans a broad energy range, from just above the Δ isobar through the second, third, and fourth resonance regions. These data
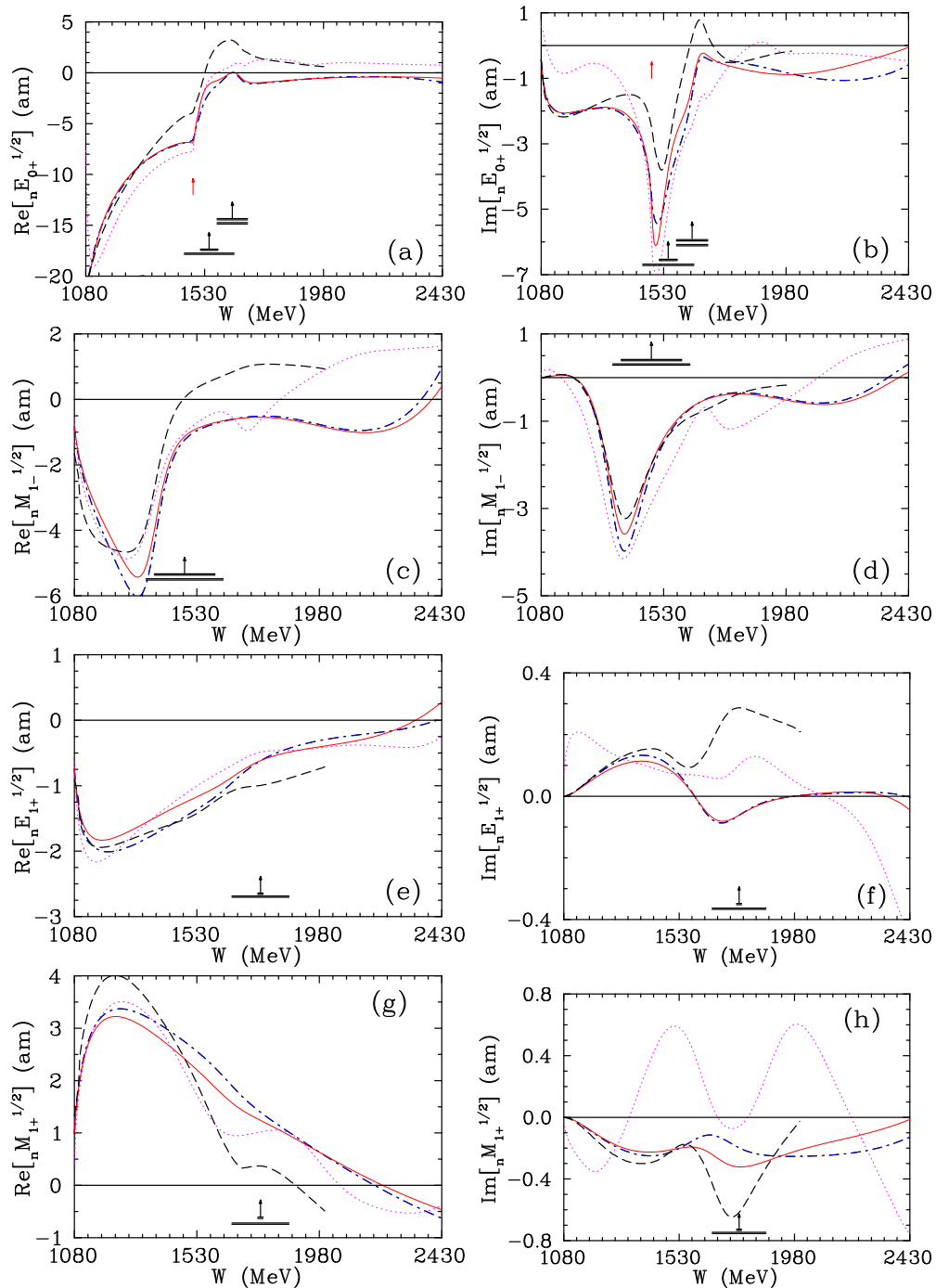
FIG. 17. Neutron multipole $I = 1/2$ amplitudes [in attometer (am) units] from threshold to $W = 2.43$ GeV ($E_\gamma = 2.7$ GeV). For the amplitudes, the subscript n denotes a neutron target, the subscript $\ell\pm$ gives the value of $j = \ell \pm 1/2$, and the superscript gives the isospin index. The red solid (blue dash-dotted) lines correspond to the new SAID MA27 (old PR15 [30]) solution. The magenta dotted (black dashed) lines give the BG2014-02 [4] (MAID2007 [31], which terminates at $W = 2$ GeV) solution. The vertical arrows indicate the Breit-Wigner mass (W_R), and the upper and lower horizontal bars show the partial ($\Gamma_{\pi N}$) and the full (Γ) widths, respectively, of the resonances extracted by the Breit-Wigner fit of the πN data associated with the SAID solution SP06 [33]. The red vertical arrows for (a) and (b) indicate the η production threshold.

extend far into the poorly studied high-mass region above $W \sim 1.8$ GeV where many resonances are expected to exist but have not been firmly established. The precision of the data can be seen not only in the presented differential cross sections, but also through the uncertainties on the extracted Legendre coefficients. This approach of fitting the excitation functions with a Legendre series presents the data in a more compact and visual manner. These results will be useful for
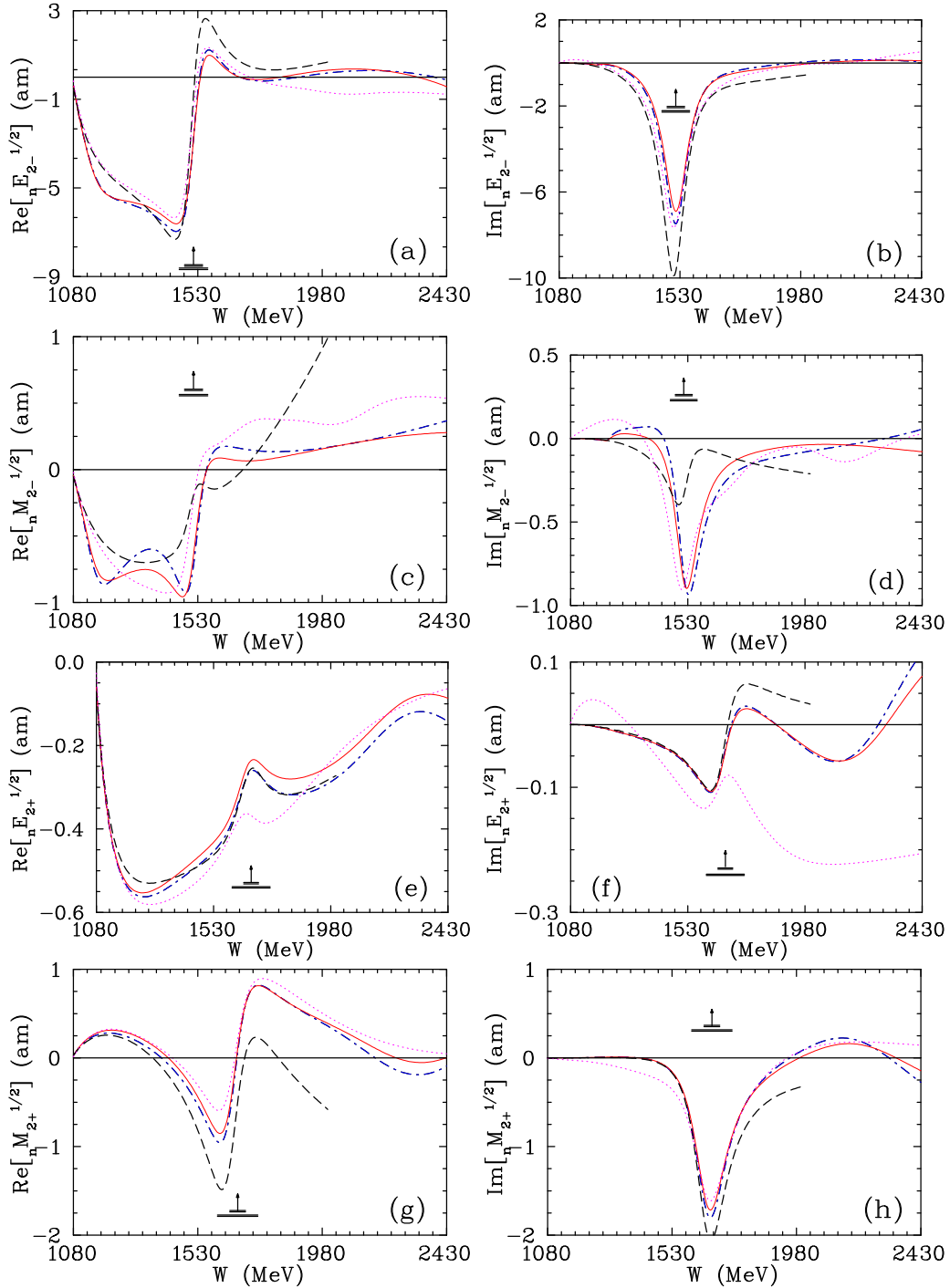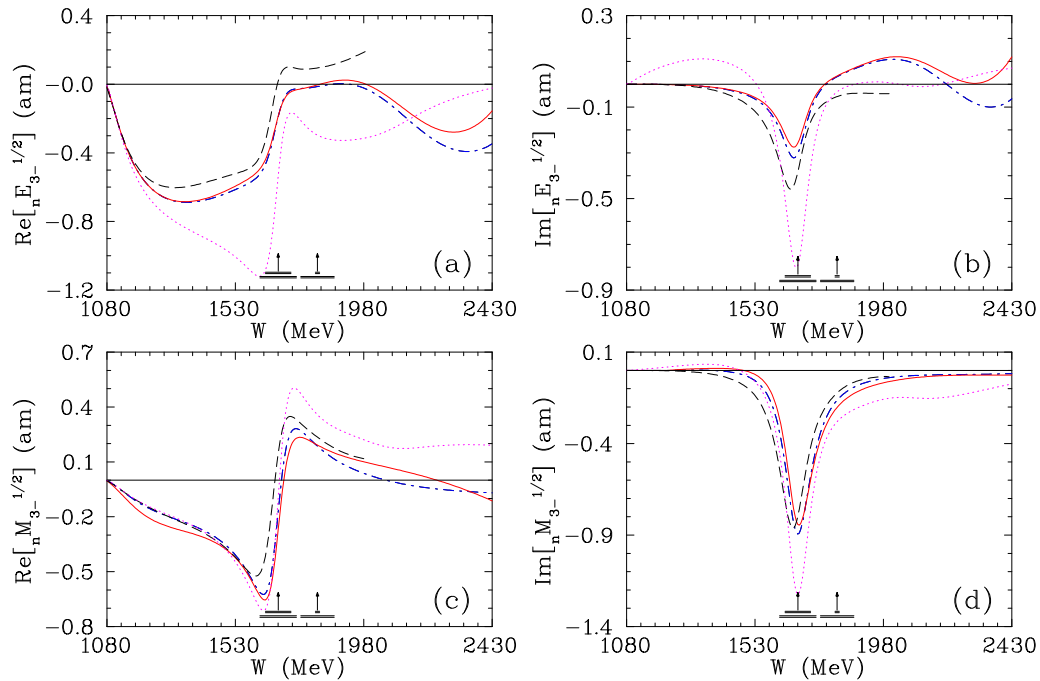
FIG. 18. Neutron multipole $I = 1/2$ amplitudes [in attometer (am) units] from threshold to $W = 2.43$ GeV ($E_\gamma = 2.7$ GeV). The notation of the multipoles is the same as in Fig. 17.

performing detailed phase shift analyses to better understand the resonant amplitudes.

On the experimental side, further improvements in the partial wave analyses await more precision data, specifically in the region above $E_\gamma = 0.5$ GeV involving polarized photons and/or polarized targets. The data that are presently available are provided in Ref. [6]. Due to the closing of

hadron facilities, new $\pi^- p \rightarrow \gamma n$ experiments are not planned, and only $\gamma n \rightarrow \pi^- p$ measurements are possible at electromagnetic facilities using deuterium targets. The agreement of these new $\gamma n \rightarrow \pi^- p$ cross section data with existing inverse π^- photoproduction measurements indicates that these g13 measurements are reliable despite the use of deuterium as an effective neutron target.

FIG. 19. Neutron multipole $I = 1/2$ amplitudes [in attometer (am) units] from threshold to $W = 2.43$ GeV ($E_\gamma = 2.7$ GeV). The notation of the multipoles is the same as in Fig. 17.

As part of this new dataset for $\gamma n \to \pi^- p$, a new SAID multipole analysis called MA27 has been completed. This energy-dependent solution, which includes the CLAS g13 data, provides an improved understanding of the N^* resonance parameters for several states, compared to the previous GB12 SAID solution that does not include the g13 CLAS data. In the MA27 solution, several photodecay amplitudes $N^* \to \gamma n$ have been extracted at their pole positions on the complex plane with very small uncertainties. This is the first-ever determination of the excited neutron multipoles for the $N(1440)1/2^+$, $N(1535)1/2^-$, $N(1650)1/2^-$, and $N(1720)3/2^+$ resonances, contributing a crucial complement to the excited proton spectra. In addition, these new precision $\gamma n \to \pi^- p$ data will provide important and necessary constraints to advance coupled-channel analysis fits that are sorely lacking γn data over nearly the full nucleon resonance region.

TABLE III. Moduli [in $(GeV)^{-1/2}$] and phases (in degrees) of the neutron helicity amplitudes $A_{1/2}(n)$ and $A_{3/2}(n)$ from the SAID MA27 solutions (third column). The Breit-Wigner neutron photodecay amplitudes are compared from SAID GB12 [8] (fourth column) from BG2013 [47] (fifth column), and from MAID2007 [31] (sixth column). The relativized quark model predictions from Ref. [48] (seventh column) are included along with the PDG values (eighth column) [2].

Resonance	Coupling	MA27 modulus, phase	GB12	BG2013	MAID2007	Capstick	PDG 2016
$N(1440)1/2^+$	$A_{1/2}(n)$	0.065 ± 0.005, $5° \pm 3°$	0.048 ± 0.004	0.043 ± 0.012	0.054	-0.006	0.040 ± 0.010
$N(1535)1/2^-$	$A_{1/2}(n)$	-0.055 ± 0.005, $5° \pm 2°$	-0.058 ± 0.006	-0.093 ± 0.011	-0.051	-0.063	-0.075 ± 0.020
$N(1650)1/2^-$	$A_{1/2}(n)$	0.014 ± 0.002, $-30° \pm 10°$	-0.040 ± 0.010	0.025 ± 0.020	0.009	-0.035	-0.050 ± 0.020
$N(1720)3/2^+$	$A_{1/2}(n)$	-0.016 ± 0.006, $10° \pm 5°$		-0.080 ± 0.050	-0.003	0.004	-0.080 ± 0.050
$N(1720)3/2^+$	$A_{3/2}(n)$	0.017 ± 0.005, $90° \pm 10°$		-0.140 ± 0.065	-0.031	0.011	-0.140 ± 0.065

[1] A. V. Anisovich *et al.*, Eur. Phys. J. A **52**, 284 (2016).

[2] C. Patrignani *et al.* (Particle Data Group), Chin. Phys. C **40**, 100001 (2016).

[3] D. Röchen, M. Döring, H. Haberzettl, J. Haidenbauer, U.-G. Meißner, and K. Nakayama, Eur. Phys. J. A **51**, 70 (2015).

[4] The Bonn-Gatchina analyses are available through the Bonn website: http://pwa.hiskp.uni-bonn.de/; see also E. Gutz *et al.*, Eur. Phys. J. A **50**, 74 (2014).

[5] H. Kamano, S. X. Nakamura, T. S. H. Lee, and T. Sato, Phys. Rev. C **88**, 035209 (2013).

[6] W. J. Briscoe, I. I. Strakovsky, and R. L. Workman, GWU CNS DAC SAID database located at http://gwdac.phys.gwu.edu/analysis/pr_analysis.html

[7] P. Nadel-Turonski, B. L. Berman, Y. Ilieva, D. G. Ireland, and A. Tkabladze, Few-Body Syst. **43**, 227 (2008).

[8] W. Chen, H. Gao, W. J. Briscoe, D. Dutta, A. E. Kudryavtsev, M. Mirazita, M. W. Paris, P. Rossi, S. Stepanyan, I. I. Strakovsky, V. E. Tarasov, and R. L. Workman, Phys. Rev. C **86**, 015206 (2012); W. Chen *et al.* (CLAS Collaboration), Phys. Rev. Lett. **103**, 012301 (2009).

[9] *N* Resonances in Pseudoscalar-Meson Photoproduction from Polarized Neutrons in $\vec{H} \cdot \vec{D}$ and a Complete Determination of the $\gamma n \to K^0 \Lambda$ Amplitude*, spokespersons F. Klein and A. Sandorfi (CLAS Collaboration), JLab Proposal E06–101, Newport News, VA, USA, 2006; *Pion Photoproduction from a Polarized Target*, Spokespersons: N. Benmouna, W. J. Briscoe, I. I. Strakovsky, S. Strauch, and G. V. O'Rielly (CLAS Collaboration), JLab Proposal E03–105, Newport News, VA, USA, 2003.

[10] *Meson Production off the Deuteron. II*, spokespersons W. J. Briscoe, V. V. Kulikov, K. Livingston, and I. I. Strakovsky (MAMI A2 Collaboration), MAMI Proposal MAMI-A2-02/13, Mainz, Germany, 2013; *Meson Production off the Deuteron. I*, spokespersons W. J. Briscoe and I. I. Strakovsky (A2 Collaboration at MAMI), MAMI Proposal MAMI-A2-02/12, Mainz, Germany, 2012.

[11] B. A. Mecking *et al.*, Nucl. Instrum. Methods Phys. Res., Sect. A **503**, 513 (2003).

[12] D. I. Sober *et al.*, Nucl. Instrum. Methods Phys. Res., Sect. A **440**, 263 (2000).

[13] M. D. Mestayer *et al.*, Nucl. Instrum. Methods Phys. Res., Sect. A **449**, 81 (2000).

[14] Y. G. Sharabian *et al.*, Nucl. Instrum. Methods Phys. Res., Sect. A **556**, 246 (2006).

[15] E. S. Smith *et al.*, Nucl. Instrum. Methods Phys. Res., Sect. A **432**, 265 (1999).

[16] G. S. Adams *et al.*, Nucl. Instrum. Methods Phys. Res., Sect. A **465**, 414 (2001).

[17] M. Amarian *et al.*, Nucl. Instrum. Methods Phys. Res., Sect. A **460**, 239 (2001).

[18] M. Lacombe, B. Loiseau, R. Vinh Mau, J. Côté, and P. Pirés, Phys. Lett. B **101**, 139 (1981).

[19] P. T. Mattione and D. S. Carman, CLAS–Note 2017–001 (2017). https://misportal.jlab.org/ul/Physics/Hall-B/clas/viewFile.cfm/2017-001.pdf?documentId=754

[20] J. Ball and E. Pasyuk, Jefferson Lab CLAS-Note 2005-002 (2005). https://misportal.jlab.org/ul/Physics/Hall-B/clas/viewFile.cfm/2005-002.pdf?documentId=24

[21] R. Schumacher, CLAS–Note 2001–010 (2001), https://www.jlab.org/Hall-B/notes/clas_notes01/01-010.pdf.

[22] CLAS physics database, http://clasweb.jlab.org/physicsdb.

[23] P. E. Scheffler and P. L. Walden, Nucl. Phys. B **75**, 125 (1974).

[24] P. Benz *et al.*, Nucl. Phys. B **65**, 158 (1973).

[25] W. J. Briscoe, A. E. Kudryavtsev, P. Pedroni, I. I. Strakovsky, V. E. Tarasov, and R. L. Workman, Phys. Rev. C **86**, 065207 (2012).

[26] M. Beneventano, S. D'Angelo, F. de Notaristefani, P. Monacelli, L. Paoluzi, A. Proia, F. Sebastiani, and M. Severi, Nuovo Cimento A **19**, 529 (1974).

[27] A. Shafi *et al.* (Crystal Ball Collaboration), Phys. Rev. C **70**, 035204 (2004).

[28] A. J. Weiss, D. J. Blasberg, J. C. Comiso, R. P. Haddock, B. M. K. Nefkens, L. J. Verhey, M. B. Zeller, K. M. Crowe, A. Fainberg, and P. Truoel, Nucl. Phys. B **101**, 1 (1975).

[29] G. J. Kim, J. Arends, W. J. Briscoe, J. Engelage, B. M. K. Nefkens, M. E. Sadler, and H. J. Ziock, Phys. Rev. D **40**, 244 (1989).

[30] P. Adlarson *et al.* (A2 Collaboration), Phys. Rev. C **92**, 024617 (2015).

[31] The MAID analyses are available through the Mainz website: http://wwwkph.kph.uni-mainz.de/MAID/; see also D. Drechsel, S. S. Kamalov, and L. Tiator, Eur. Phys. J. A **34**, 69 (2007).

[32] V. E. Tarasov, W. J. Briscoe, H. Gao, A. E. Kudryavtsev, and I. I. Strakovsky, Phys. Rev. C **84**, 035203 (2011).

[33] R. A. Arndt, W. J. Briscoe, I. I. Strakovsky, and R. L. Workman, Phys. Rev. C **74**, 045205 (2006).

[34] R. A. Arndt, W. J. Briscoe, I. I. Strakovsky, and R. L. Workman, Phys. Rev. C **76**, 025209 (2007).

[35] M. Dugger *et al.* (CLAS Collaboration), Phys. Rev. C **76**, 025211 (2007).

[36] R. Machleidt, K. Holinde, and C. Elster, Phys. Rep. **149**, 1 (1987).

[37] Ya. I. Azimov, I. I. Strakovsky, W. J. Briscoe, and R. L. Workman, Phys. Rev. C **95**, 025205 (2017).

[38] M. Dugger *et al.* (CLAS Collaboration), Phys. Rev. C **88**, 065203 (2013).

[39] R. A. Arndt, J. M. Ford, and L. D. Roper, Phys. Rev. D **32**, 1085 (1985).

[40] R. L. Workman, M. W. Paris, W. J. Briscoe, and I. I. Strakovsky, Phys. Rev. C **86**, 015202 (2012).

[41] F. Adamyan *et al.*, J. Phys. G: Nucl. Phys. **14**, 835 (1988); L. Abrahamian *et al.*, Sov. J. Nucl. Phys. **32**, 69 (1980).

[42] G. Mandaglio *et al.* (GRAAL Collaboration), Phys. Rev. C **82**, 045209 (2010); G. Giardina (private communication).

[43] J. Alspector, D. Fox, D. Luckey, C. Nelson, L. S. Osbourne, G. Tarnopolsky, Z. Bar-Yam, J. de Pagter, J. Dowd, W. Kern, and S. M. Matin, Phys. Rev. Lett. **28**, 1403 (1972).

[44] D. Ho *et al.* (CLAS Collaboration), Phys. Rev. Lett. **118**, 242002 (2017).

[45] A. Svarc, M. Hadzimehmedovic, H. Osmanovic, J. Stahov, L. Tiator, and R. L. Workman, Phys. Rev. C **89**, 065208 (2014).

[46] R. L. Workman, L. Tiator, and A. Sarantsev, Phys. Rev. C **87**, 068201 (2013).

[47] A. V. Anisovich, V. Burkert, E. Klempt, V. A. Nikonov, A. V. Sarantsev, and U. Thoma, Eur. Phys. J. A **49**, 67 (2013).

[48] S. Capstick, Phys. Rev. D **46**, 2864 (1992).

[49] R. A. Arndt, W. J. Briscoe, I. I. Strakovsky, and R. L. Workman, Phys. Rev. C **66**, 055213 (2002).